

# Study of the $^{44}\text{Ti}(\alpha, \text{p})^{47}\text{V}$ reaction rate using high precision $^{50}\text{Cr}(\text{p}, \text{t})^{48}\text{Cr}$ measurements

Sifundo Delton Binda



A dissertation submitted to the Faculty of Science, University of the Witwatersrand, Johannesburg, in fulfilment of the requirements for the degree of Master of Science.

School of Physics

Faculty of Science

University of the Witwatersrand

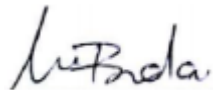
11 March 2022, Johannesburg, South Africa

Supervisor : Dr Luna Pellegrini  
Co-Supervisors: Dr Philip Adsley  
: Prof. Mathis Wiedeking  
: Prof. Elias Sideras-Haddad

This work is based on the research supported in part by the National Research Foundation of South Africa (Grant Number: 118846).

# Declaration

I, Sifundo Delton Binda, declare that this dissertation is my own unaided work. It is being submitted for Masters of Science degree to the University of the Witwatersrand, Johannesburg. It has not been submitted previously for any degree or examination to any other university.

A handwritten signature in black ink, appearing to read 'Sifundo Binda', written in a cursive style.

(Signature of candidate)

11 March 2022

# Study of the $^{44}\text{Ti}(\alpha,\text{p})^{47}\text{V}$ reaction rate using high precision $^{50}\text{Cr}(\text{p},\text{t})^{48}\text{Cr}$ measurements

Sifundo Delton Binda

School of Physics

Faculty of Science

University of the Witwatersrand, Johannesburg, South Africa

Dissertation: Master of Science

## Abstract

Formed in a region where most material is captured onto the compact object remaining at the end of the collapse, the observation of  $^{44}\text{Ti}$  offers the best diagnostic tool for Core-Collapse Supernovae. The destruction of  $^{44}\text{Ti}$  is controlled by the  $^{44}\text{Ti}(\alpha,\text{p})^{47}\text{V}$  reaction. Direct measurements are challenging due to the low cross sections and radioactive ion beam intensities so statistical models are used to predict reaction rates. Predictions for  $\alpha$ -induced reactions on  $N=Z$  nuclei might not be reliable due to the lower effective level density in the compound nucleus. High resolution  $0^\circ$   $^{50}\text{Cr}(\text{p},\text{t})^{48}\text{Cr}$  measurements were performed using the K600 magnetic spectrometer at iThemba LABS to identify natural parity levels in  $^{48}\text{Cr}$ . The number of levels observed was compared to level-density calculations, indicating a theoretical overestimation of the level density. Further work is required to better understand the implications of this for the reaction rate.

THIS WORK IS DEDICATED TO MY FAMILY.

# Acknowledgements

First and foremost, I would like to thank my supervisors; Dr Luna Pellegrini and Dr Philip Adsley. Your supervision made my MSc journey an enjoyable ride. Your unparalleled support and guidance is what kept me going, it nurtured my interest in physics and made me a better student. I have learnt and continue to learn a lot from both of you. To my other supervisor, Prof. Mathis Wiedeking, thank you for the advice provided in the draft of this dissertation and always asking the right questions which has brought me greater awareness into my work. My deepest gratitude goes to Prof. Elias Sideras-Haddad whom I've worked with since undergrad, and introduced me to the amazing K600 team. To all of you, I say *Asante sana*.

To my family and friends who have been with me since day one. You've encouraged me all the way. Thank you for the love and support. A special thanks goes to the iThemba LABS students, whose laughter and company have kept me sane for these two years of lockdown.

None of this work would have been possible without the knowledge and expertise of the physicists and students from iThemba LABS and the University of Notre Dame involved in the PR242 experiment and its data collection. Thank you for ensuring the integrity and usability of the data used in this dissertation.

I would like to acknowledge iThemba LABS Top-up bursary and the National Research Foundation of South Africa (Grant Number: 118846) for providing me with the funds that enabled the completion of this dissertation.

# Contents

<b>Abstract</b>	<b>ii</b>
<b>Acknowledgements</b>	<b>iv</b>
<b>List of Figures</b>	<b>ix</b>
<b>List of Tables</b>	<b>x</b>
<b>1 Scientific motivation</b>	<b>1</b>
1.1 Introduction . . . . .	1
1.2 Astrophysical background . . . . .	1
1.3 Sensitivity and experimental studies of the $^{44}\text{Ti}(\alpha,p)^{47}\text{V}$ reaction . . . . .	3
1.3.1 Sensitivity studies on $^{44}\text{Ti}$ . . . . .	3
1.3.2 Experimental studies: $^{44}\text{Ti}(\alpha,p)^{47}\text{V}$ . . . . .	3
1.3.3 Uncertainties in the HF model . . . . .	3
1.4 The present work . . . . .	4
1.4.1 $^{50}\text{Cr}(p,t)^{48}\text{Cr}$ measurements . . . . .	4
1.4.1.1 (p,t) measurements using the K600 magnetic spectrometer . . . . .	6
<b>2 Theoretical considerations</b>	<b>7</b>
2.1 Introduction . . . . .	7
2.2 Nuclear reaction rates . . . . .	7
2.3 Statistical models . . . . .	9
2.3.1 Compound nucleus model . . . . .	9
2.3.2 Hauser-Feshbach model . . . . .	10
2.3.3 Nuclear level densities . . . . .	11
<b>3 Experimental setup</b>	<b>13</b>
3.1 Introduction . . . . .	13
3.2 The iThemba LABS accelerator facility . . . . .	13
3.3 Scattering chamber . . . . .	14

3.4	The K600 magnetic spectrometer . . . . .	16
3.5	Focal-plane detectors . . . . .	19
3.5.1	Vertical Drift Chambers . . . . .	19
3.5.2	Plastic Scintillators . . . . .	21
3.6	Electronics and DAQ . . . . .	22
3.6.1	Trigger logic . . . . .	22
3.6.2	Pre-amplifiers and TDCs . . . . .	24
3.6.3	DAQ . . . . .	24
<b>4</b>	<b>Data Analysis</b>	<b>25</b>
4.1	Introduction . . . . .	25
4.2	Data Extraction . . . . .	25
4.2.1	Particle Identification . . . . .	25
4.2.2	Focal-plane event reconstruction . . . . .	26
4.2.2.1	Cable lengths . . . . .	26
4.2.2.2	LUT . . . . .	28
4.2.2.3	LUT offsets . . . . .	28
4.2.2.4	Scattering angle calibration . . . . .	31
4.3	Data Optimisation and Calibration . . . . .	34
4.3.1	Line-shape corrections . . . . .	34
4.3.2	Energy calibration . . . . .	36
4.3.2.1	Position to momentum calibration . . . . .	38
4.3.2.2	Momentum to energy conversion . . . . .	39
4.3.2.3	The excitation energy spectra of $^{22}\text{Mg}$ . . . . .	40
4.4	The excitation energy spectra of $^{48}\text{Cr}$ . . . . .	41
4.4.1	Contaminant states . . . . .	42
4.4.1.1	Carbon contaminants . . . . .	43
4.4.1.2	Oxygen contaminants . . . . .	43
4.4.1.3	Background . . . . .	43
4.4.2	Low-lying states in $^{48}\text{Cr}$ . . . . .	45
<b>5</b>	<b>Results and Discussion</b>	<b>47</b>
5.1	Level structure of $^{48}\text{Cr}$ . . . . .	47
5.1.1	States below the $\alpha$ -threshold . . . . .	47
5.1.2	States above the $\alpha$ -threshold . . . . .	50
5.2	Nuclear-level cumulatives . . . . .	52
<b>6</b>	<b>Conclusion and Outlook</b>	<b>55</b>

<b>A Target energy loss calculations</b>	<b>56</b>
<b>Bibliography</b>	<b>63</b>

# List of Figures

1.1	Partial decay scheme of $^{44}\text{Ti}$ . . . . .	2
1.2	Schematic diagram of a massive star (mass $\geq 8 M_{\odot}$ ). . . . .	2
1.3	Sketch of the $^{50}\text{Cr}(p,t)^{48}\text{Cr}$ and $^{44}\text{Ti}(\alpha,p)^{47}\text{V}$ reactions forming the $^{48}\text{Cr}$ compound nucleus. . . . .	5
1.4	Schematic view of the resonant capture of $\alpha$ -particles in the $^{44}\text{Ti}(\alpha,p)^{47}\text{V}$ reaction. . . . .	5
2.1	Effective Gamow windows for $^{44}\text{Ti}(\alpha,p)^{47}\text{V}$ and the competing $^{40}\text{Ca}(\alpha,\gamma)^{44}\text{Ti}$ reaction at $T_9 = 2$ and $T_9 = 5$ . . . . .	9
3.1	Layout of the iThemba LABS SSC facility . . . . .	15
3.2	Transverse view of the new small angle scattering chamber . . . . .	16
3.3	A diagram of the K600 spectrometer . . . . .	17
3.4	TRACK v8.6 simulated triton trajectories . . . . .	17
3.5	The (p,t) beamstop . . . . .	18
3.6	The computer generated design layout of the new XU VDC detector. . . . .	20
3.7	A schematic top-view cross section of an XU VDC. . . . .	20
3.8	Plastic scintillator paddles of the K600 focal plane detector system. . . . .	22
3.9	The trigger electronics flow diagram for experiment PR242. . . . .	23
4.1	The Particle Identification spectrum . . . . .	26
4.2	TDC channel number versus TDC time spectrum . . . . .	27
4.3	TDC channel number versus TDC time spectrum . . . . .	27
4.4	Spectrum of the drift times of the X1 wire plane. . . . .	29
4.5	The lookup table (LUT) for the X1 wire plane. . . . .	29
4.6	The spectrum of drift distances. . . . .	29
4.7	An illustration of a particle trajectory through the VDC. . . . .	30
4.8	A 2D resolution plot for the X2 wire-plane . . . . .	30
4.9	The pepper-pot collimator for the small angle mode . . . . .	31
4.10	2D spectra for $\theta_{FP}$ versus $X_{FP}$ . . . . .	32

4.11 Spectra showing focal-plane trajectory angle $\theta_{FP}$ at a focal-plane position of 484 mm. . . . .	32
4.12 Graphs showing the mapping of focal plane angle ( $\theta_{FP}$ ) to scattering angle ( $\theta_{SCAT}$ ) at different focal plane positions ( $x_{FP}$ ). . . . .	33
4.13 Left: The slope as a function of focal plane position. Right: The offset as a function of focal plane position. . . . .	33
4.14 2D spectra for $\theta_{SCAT}$ versus $X_{FP}$ . . . . .	34
4.15 Line shape correction . . . . .	35
4.16 Lineshape correction model . . . . .	36
4.17 The effect of line shape correction on the $^{48}\text{Cr}$ data . . . . .	36
4.18 The corrected focal-plane position spectrum ( $x_{FP}$ ) for $^{22}\text{Mg}$ . . . . .	37
4.19 The rigidity calibration. . . . .	39
4.20 The calibrated excitation energy spectra of $^{22}\text{Mg}$ . . . . .	41
4.21 The excitation energy spectra of $^{48}\text{Cr}$ . . . . .	42
4.22 Tritons $B\rho$ map . . . . .	43
4.23 Mylar(p,t) spectra (red) superimposed on the $^{50}\text{Cr}(p,t)$ spectra (black) using $^{12}\text{C}(p,t)^{10}\text{C}$ reaction kinematics. . . . .	44
4.24 Mylar(p,t) spectra (red) superimposed on the $^{50}\text{Cr}(p,t)$ spectra (black) using $^{16}\text{O}(p,t)^{14}\text{O}$ reaction kinematics. . . . .	44
4.25 Residual energy plot . . . . .	45
5.1 Excited states below the $\alpha$ -threshold in $^{48}\text{Cr}$ . . . . .	49
5.2 Excited states above the $\alpha$ -threshold in $^{48}\text{Cr}$ . . . . .	50
5.3 Nuclear level cumulatives in $^{48}\text{Cr}$ . . . . .	53
A.1 Target geometry of the $^{50}\text{Cr}$ target used in this experiment. . . . .	57
A.2 Graphs of energy and projected range. . . . .	58

# List of Tables

3.1	List of targets used the experiment and their purposes. . . . .	15
3.2	The ion-optic matrix elements of the K600 magnetic spectrometer. . . . .	19
3.3	Efficiencies of the VDC wire planes for the chained $^{50}\text{Cr}(p,t)^{48}\text{Cr}$ runs. . . . .	21
3.4	Beamtime tally on targets used during the experiment. . . . .	22
4.1	Look up table offsets. . . . .	31
4.2	Angle calibration parameters. . . . .	33
4.3	Lineshape correction parameters for Equation 4.5. . . . .	37
4.4	The focal-plane positions of tritons following a $^{24}\text{Mg}(p,t)^{22}\text{Mg}$ reaction. . . . .	38
4.5	Focal-plane position and corresponding $B\rho$ values for the $^{24}\text{Mg}(p,t)^{22}\text{Mg}$ reaction. . . . .	39
4.6	Focal-plane position to momentum calibration parameters . . . . .	39
4.7	A comparison of the energy values for the excited states of $^{22}\text{Mg}$ . . . . .	40
4.8	Systematic uncertainty budget for $^{22}\text{Mg}$ . . . . .	41
4.9	Q-values of different reactions on targets used in the experiment. . . . .	42
4.10	Energy values of the low-lying excited states of $^{48}\text{Cr}$ . . . . .	45
4.11	Systematic uncertainty budget . . . . .	46
5.1	List of states in $^{48}\text{Cr}$ below the $\alpha$ -threshold. . . . .	48
5.2	List of states in $^{48}\text{Cr}$ above the $\alpha$ -threshold. . . . .	51
5.3	Energy values of the first 7 excited states of $^{48}\text{Cr}$ . . . . .	52
A.1	Table showing the parameters of the energy loss models. . . . .	57

# Chapter 1

## Scientific motivation

### 1.1 Introduction

The evolution of core-collapse supernovae (CCSNe) depends on a number of nuclear reactions consuming and producing freshly synthesised radionuclides. One such radioisotope that can help us to understand CCSNe is  $^{44}\text{Ti}$ , a radioactive isotope with a half-life of 59 years.  $^{44}\text{Ti}$  decays primarily by electron capture into excited states in  $^{44}\text{Sc}$  which undergo further radioactive decay into the excited states of  $^{44}\text{Ca}$  (see Figure 1.1). The  $\gamma$ -rays from  $^{44}\text{Sc}$  and  $^{44}\text{Ca}$  may be observed using  $\gamma$ -ray telescopes [1].  $^{44}\text{Ti}$  is believed to be produced during the  $\alpha$ -rich freeze-out expansion phase from inside the silicon-burning envelope (see Figure 1.2) of CCSNe progenitors, a region that marks the transition between material that is captured onto the compact object remaining at the end of the collapse and material that is ejected during the explosion [2]. Since most material from this region is captured into the compact object remaining at the end of the collapse, the observation of  $^{44}\text{Ti}$  offers the best diagnostic tool for the underlying physics of such supernovae.

### 1.2 Astrophysical background

The calculated ejected mass of  $^{44}\text{Ti}$  in supernova remnant Cassiopeia A from astronomical observations, with COMPTEL [5], BeppoSax [6], INTEGRAL [7] and NuSTAR [8], yields a mass of  $1.25 \pm 0.3 \times 10^{-4} M_{\odot}$  \* of  $^{44}\text{Ti}$  [7,8]. This mass value and that from supernova remnant 1987A [9] show that  $^{44}\text{Ti}$  is under-produced in standard, spherical supernova explosion models [10, 11]. Although the current models are falling short in the synthesis of  $^{44}\text{Ti}$ , it has been argued from discrepancies between the galactic supernovae rate and the observed sources of  $^{44}\text{Ti}$  in the all-sky surveys that  $^{44}\text{Ti}$ -producing supernova are the exception not the norm [12, 13].

---

\*The solar mass ( $M_{\odot}$ ) is a standard unit of mass in astronomy, equal to approximately  $2 \times 10^{30}$  kg.

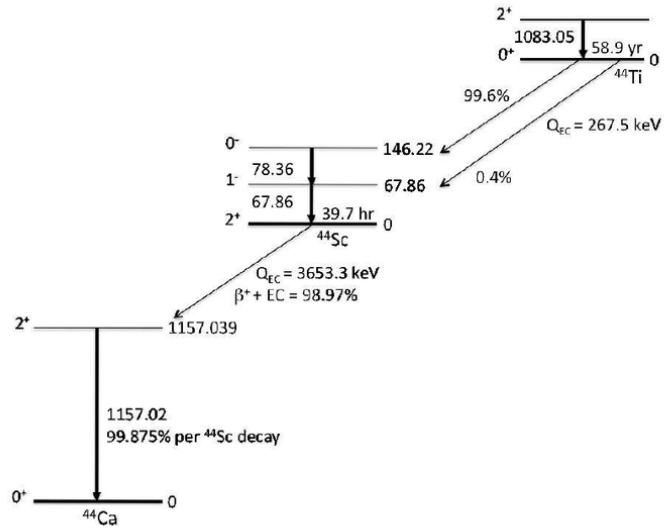


Figure 1.1: Partial decay scheme of  $^{44}\text{Ti}$  [3].

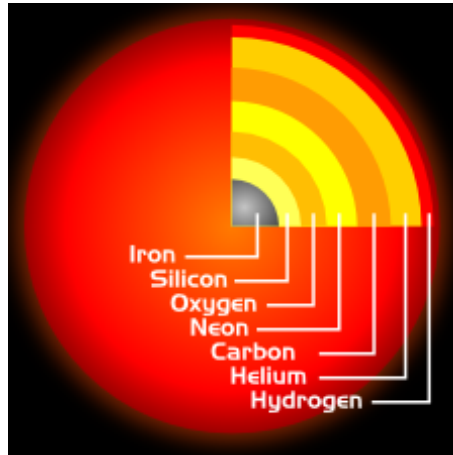


Figure 1.2: Schematic diagram of a massive star (mass  $\geq 8 M_{\odot}$ ) with its onion-layered envelopes marking the ashes of the different burning stages of the star, from hydrogen burning to the silicon burning, ultimately forming a nickel-iron core [4].

A possible reason behind the enhanced production of  $^{44}\text{Ti}$  in observations as compared to model calculations may be due to the asymmetry of supernovae explosion. Two-dimension asymmetric explosion models performed by Nagataki et al. [14] show that the bipolar explosion scenario could account for the enhancement of  $^{44}\text{Ti}$  production along the poles, and evidence of an asymmetric explosion mechanism has recently been observed in the spatial mapping of  $^{44}\text{Ti}$  in Cassiopeia A by NuSTAR [8]. To address ideas such as  $^{44}\text{Ti}$ -producing supernovae being an anomaly or asymmetric explosion scenarios and to use the ejected mass as a probe, it is necessary to precisely understand the synthesis of  $^{44}\text{Ti}$ .

## 1.3 Sensitivity and experimental studies of the $^{44}\text{Ti}(\alpha, \text{p})^{47}\text{V}$ reaction

### 1.3.1 Sensitivity studies on $^{44}\text{Ti}$

The amount of  $^{44}\text{Ti}$  produced in CCSNe has been shown to be strongly dependent on a number of nuclear reactions, most importantly the  $^{44}\text{Ti}(\alpha, \text{p})^{47}\text{V}$  which controls the destruction of  $^{44}\text{Ti}$  as shown in the sensitivity studies performed by Magkotsios et al. [15] and The et al. [12]. From these studies it's shown that the final mass fraction of  $^{44}\text{Ti}$  depends strongly on the  $^{44}\text{Ti}(\alpha, \text{p})^{47}\text{V}$  rate. As this reaction falls out of equilibrium, the  $^{44}\text{Ti}$  mass fraction departs from the local quasi-statistical equilibrium (QSE) structure. Since this reaction determines the temperature at which  $^{44}\text{Ti}$  departs from the QSE mass fraction curve, it has a direct effect on the final  $^{44}\text{Ti}$  mass fraction.

### 1.3.2 Experimental studies: $^{44}\text{Ti}(\alpha, \text{p})^{47}\text{V}$

There have been only two experiments investigating this reaction at astrophysically relevant energies ( $E_{c.m.} = 2.1 - 6.1$  MeV): Sonzogni et al. [16] and Margerin et al. [17]. The two experiments were inverse kinematics reactions with radioactive beams of  $^{44}\text{Ti}$  incident on a  $^4\text{He}$  gas target. Radioactive beam contaminants and extremely low cross sections within this energy window were the main experimental challenges. Additionally, the Margerin et al. data suffered from considerable amount of background coming from reactions on the gas cell, even without the  $^4\text{He}$  gas for the reaction of interest. This background spanned the region of interest and constrained them to produce only a limit on the cross section instead of a determinant value. Lacking cross-sections in the relevant window, the calculated  $^{44}\text{Ti}(\alpha, \text{p})^{47}\text{V}$  reaction rate used in stellar models is based on statistical Hauser-Feshbach (HF) model predictions.

### 1.3.3 Uncertainties in the HF model

The HF formalism [18] rests upon the hypothesis that populated states in a compound nucleus form a continuum - an overlap of nuclear levels because they are so many that their spacing is much less than the widths of the individual nuclear levels [19] - and that the outgoing channel after the formation of a compound nucleus is independent of the incoming channel that created the compound nucleus. It is generally understood that for a HF model to give a reliable prediction of a reaction rate, the average level spacing, ( $D$ ) has to be smaller than, or similar to, the average resonance width ( $\langle \Gamma \rangle$ ),

$$D = \frac{1}{\rho(E, J, \pi)} \leq \langle \Gamma \rangle \quad (1.1)$$

in each partial wave [20]. In the equation,  $\rho(E, J, \pi)$  represents the level density. However, this might not be suitable for  $\alpha$ -capture reactions on even-even nuclei where the effective level spacing increases because only isoscalar natural-parity resonances in the compound nucleus participate, limiting the effective level density. When the HF model is applied for a compound nucleus where the level density is not sufficiently large, the statistical model calculation results in a misestimation of the actual reaction cross-section and therefore, reaction rate.

Constraints on the  $^{44}\text{Ti}(\alpha, \text{p})^{47}\text{V}$  reaction rate have been recently studied in the work of Chippis et al. [21]. The work accessed the available data on the reaction and compared it to statistical models using standard optical model parameters to constrain the reaction rate across a temperature range. However, uncertainties remain, due to the lack of experimental data on resonance level contributions and cross-sections which are required to allow for a direct comparison to the HF model.

## 1.4 The present work

The compound nucleus of the  $^{44}\text{Ti}(\alpha, \text{p})^{47}\text{V}$  reaction is  $^{48}\text{Cr}$  (see Figures 1.3 and 1.4).  $^{48}\text{Cr}$  is an even-even nucleus, with a ground state spin-parity of  $J^\pi = 0^+$ . Spectroscopic information on this nucleus is scarce especially in the region of astrophysical importance. With no experimental information to infer resonance level contributions from, the level densities used in the HF model are based on theoretical models. From this knowledge, the present experiment was proposed at iThemba LABS to indirectly study the  $^{44}\text{Ti}(\alpha, \text{p})^{47}\text{V}$  reaction by precisely measuring the excitation energies  $\alpha$ -unbound natural parity states in  $^{48}\text{Cr}$ . It is these natural parity states in  $^{48}\text{Cr}$  that can act as resonances in the  $^{44}\text{Ti}(\alpha, \text{p})^{47}\text{V}$  reaction. The main goal of this present work is aimed at obtaining, for the first time, precise energies of the  $\alpha$ -unbound states in the compound nucleus,  $^{48}\text{Cr}$ . This is achieved by creating the  $^{48}\text{Cr}$  compound nucleus of the desired  $^{44}\text{Ti}(\alpha, \text{p})^{47}\text{V}$  reaction, through a  $^{50}\text{Cr}(\text{p}, \text{t})^{48}\text{Cr}$  reaction (see Figure 1.3).

### 1.4.1 $^{50}\text{Cr}(\text{p}, \text{t})^{48}\text{Cr}$ measurements

The use of the two-neutron pick up reaction, (p,t), to study the level structure of  $^{48}\text{Cr}$  is ideal since for high proton beam energies it excites mainly natural parity states in  $^{48}\text{Cr}$ , the same states that would be expected to be excited in a  $^{44}\text{Ti}(\alpha, \text{p})^{47}\text{V}$  reaction. This occurs because, during a double pick-up reaction as this one, a neutron pair ( $S=0$ ) is removed from  $^{50}\text{Cr}$  which has a spin-parity of  $0^+$  in its ground state and this leaves behind a  $^{48}\text{Cr}$  isotope with mainly natural-parity states excited. The spin and parity of the states in the recoil  $^{48}\text{Cr}$  are solely determined by the orbital angular momentum transfer, thus only natural

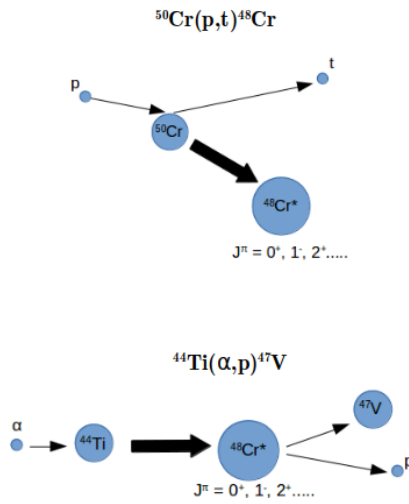


Figure 1.3: Sketch of the  $^{50}\text{Cr}(p,t)^{48}\text{Cr}$  and  $^{44}\text{Ti}(\alpha,p)^{47}\text{V}$  reactions forming the  $^{48}\text{Cr}$  compound nucleus.

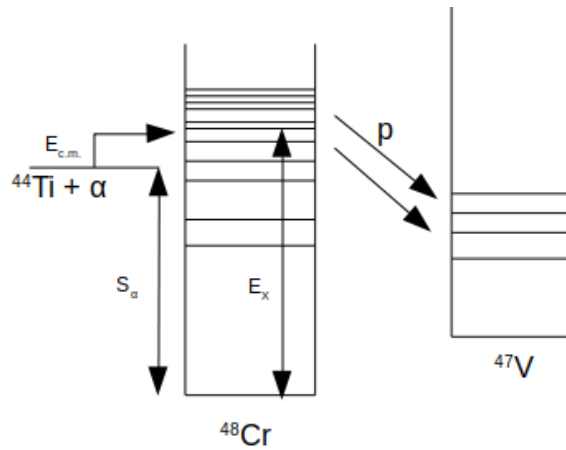


Figure 1.4: Schematic view of the resonant capture of  $\alpha$ -particles in the  $^{44}\text{Ti}(\alpha,p)^{47}\text{V}$  reaction.  $E_{c.m.}$  is the center-of-mass energy,  $S_\alpha$  is the  $Q$ -value of the radiative capture reaction (see text) and  $E_x$  is the excitation energy.

parity states will be populated through this direct mechanism. It should be noted that this reaction mechanism competes with a  $S \neq 0$ , multistep process :  $^{50}\text{Cr}(p,d)^{49}\text{Cr}(d,t)^{48}\text{Cr}$  [22]. However, this reaction mechanism is much weaker than the pair transfer at higher proton incident energies. Evidence of the selectivity of the (p,t) reaction at 100 MeV proton beam energies has been observed in previous experiments with well known natural parity states being strongly favored [23, 24].

#### 1.4.1.1 (p,t) measurements using the K600 magnetic spectrometer

The (p,t) setup at iThemba LABS has in the past achieved an energy resolution of 35 keV in the focal plane of the K600 magnetic spectrometer [25]. With a high resolution magnetic spectrometer setup, the (p,t) allows for high energy resolution measurements in which closely spaced levels at higher energies in  $^{48}\text{Cr}$  can be resolved and identified. Using the astrophysical energy window approximation (Section 2.1), the energy range where states in  $^{48}\text{Cr}$  will be the most influential in governing the  $^{44}\text{Ti}(\alpha,\text{p})^{47}\text{V}$  reaction is  $E_{c.m.} = 2.1 - 6.1$  MeV. This translates to an excitation energy range of the astrophysically relevant states from about 9 to 14 MeV. The excitation energy is given by:

$$E_x = E_{c.m.} + S_\alpha \quad (1.2)$$

where  $E_{c.m.}$  is the center-of-mass energy, and  $S_\alpha$  is the Q-value of the radiative capture reaction:  $^{44}\text{Ti} + \alpha \rightarrow \gamma + ^{48}\text{Cr}$ , see Figure 1.4 ( $S_\alpha = 7698(7)$  keV [26]). Given that this range of interest goes up to 14 MeV in excitation energy, high energy resolution techniques are needed to resolve possible closely spaced states.

To get to the  $\alpha$ -unbound states (9 to 14 MeV in  $E_x$ ) in  $^{48}\text{Cr}$ , the  $^{50}\text{Cr}(\text{p,t})^{48}\text{Cr}$  reaction was performed at a high energy of 100 MeV to ensure a high selectivity to natural-parity states and that the tritons have enough energy to be detected at the focal plane of the K600 magnetic spectrometer following the (p,t) reaction which has a large negative Q-value of  $-15.101(7)$  MeV.

The current work will allow for the extraction of nuclear level cumulatives by the direct counting of the states in  $^{48}\text{Cr}$  through obtaining precise energies of the  $\alpha$ -unbound states in the compound nucleus. This result can be compared to theoretical level density calculation models used in the HF model.

This dissertation is structured as follows: Chapter 2 describes the theoretical background involving stellar reaction rates, the HF model and nuclear level densities. Chapter 3 describes the experimental method which includes the equipment used for this study as well as the data acquisition procedure. Chapter 4 outlines the data analysis. The experimental and theoretical results are presented and discussed in Chapter 5. Concluding remarks as well as an overview of future work is given in Chapter 6.

## Chapter 2

# Theoretical considerations

### 2.1 Introduction

Nuclear reaction cross-sections ( $\sigma(E)$ ) indicate the likelihood of a nuclear reaction taking place at a particular energy. Cross-sections are a function of energy and decrease faster than exponentially at low energies for charged particle reactions. Due to this, the experimental measurement of these cross-sections at energies available in stellar environments is hard. In the absence of experimental data, statistical models are an important substitute. Statistical models have been studied for many years with application to many nuclear reactions inaccessible via direct experimental means. However, no one has verified for in the  $^{44}\text{Ti}(\alpha, p)^{47}\text{V}$  reaction, whose compound nucleus is  $^{48}\text{Cr}$ , that such models are applicable for  $^{48}\text{Cr}$  as it is not a heavy nucleus and it is  $\alpha$ -conjugate. The applicability of these statistical models in this reaction is an important property to check. In this chapter, a brief account of the energies encountered in stellar environments, the so-called Gamow-window (Section 2.2), the statistical models and its ingredients (Section 2.3) are presented.

### 2.2 Nuclear reaction rates

The energy ( $E$ ) averaged nuclear reaction rate per particle pair at a given stellar temperature  $T$  is determined by folding the reaction cross section with the Maxwell-Boltzmann velocity distribution of the projectile [27]:

$$\langle \sigma v \rangle = \left( \frac{8}{\pi \mu} \right)^{1/2} \left( \frac{1}{kT} \right)^{1/2} \int_0^{\infty} E \sigma(E) \exp\left(-\frac{E}{kT}\right) dE, \quad (2.1)$$

where  $\mu$  is the reduced mass ( $\mu = m_1 m_2 / (m_1 + m_2)$ ,  $m_1$  and  $m_2$  are the masses of the colliding particles) and  $k$  is the Boltzmann constant. Numerically, the reaction rate is given by:

$$N_A \langle \sigma v \rangle = \left( \frac{3.7318 \times 10^{10}}{T_9^{3/2}} \right) \left( \frac{1}{\hat{A}} \right)^{1/2} \int_0^\infty E \sigma(E) \exp\left(-\frac{11.605E}{T_9}\right) dE, \quad (2.2)$$

where  $N_A$  is Avogadro's number,  $T_9$  is the temperature in stellar environments in  $10^9\text{K}$  [27] and  $\hat{A}$  is the reduced atomic mass ( $\hat{A} = M_1 M_2 / (M_1 + M_2)$ ),  $M_1$  and  $M_2$  is the atomic mass of the colliding particles.

For charged particles, the cross-section is strongly suppressed at low energies due to the Coulomb barrier. The cross-section is approximated as:

$$\sigma(E) = \frac{1}{E} \exp(-2\pi\eta) S(E) \quad (2.3)$$

with  $\eta$  being the Sommerfeld parameter and  $S(E)$  the astrophysical S-factor. In this approximation,  $\sigma(E)$  is split into 2 parts; Coulomb penetration,  $\exp(-2\pi\eta)$  and the nuclear structural input,  $S(E)$ . Substituting  $\sigma(E)$  into Equation 2.1 gives:

$$\langle \sigma v \rangle = \left( \frac{8}{\pi\mu} \right)^{1/2} \left( \frac{1}{kT} \right)^{1/2} \int_0^\infty S(E) \exp\left[-\frac{E}{kT} - \frac{b}{E^{1/2}}\right] dE \quad (2.4)$$

where the term  $b = (2\mu)^{1/2} \pi e^2 Z_1 Z_2 / \hbar$  arises from the barrier penetrability. For particles having energies less than the Coulomb barrier, the product of the penetration factor and the Maxwell-Boltzmann distribution function results in the Gamow peak, in which energy region most of the reactions will take place. Taking the first derivative of the integrand yields the location of the Gamow peak,  $E_0$ , and the effective width of the energy window,  $\Delta$ :

$$E_0 = 0.122(Z_1^2 Z_2^2 \mu T_9^2)^{1/3} \text{ MeV and} \quad (2.5)$$

$$\Delta = 0.2368(Z_1^2 Z_2^2 \mu T_9^5)^{1/6} \text{ MeV, respectively,} \quad (2.6)$$

with  $Z_1$  and  $Z_2$  the charges of the involved nuclei. The location and width of the Gamow depend on the charges of the reactants, and on the temperature of the interacting plasma.

The Gamow window for the  $^{44}\text{Ti}(\alpha, p)^{47}\text{V}$  reaction is shown in Figure 2.1. The figure taken from the work of Hoffmann et al. [3], studying the competing  $^{40}\text{Ca}(\alpha, \gamma)^{44}\text{Ti}$  reaction which is not part of this work. Effective Gamow windows for  $^{44}\text{Ti}(\alpha, p)^{47}\text{V}$  are calculated at  $T_9 = 2$  and  $T_9 = 5$ . Shown are the true Gamow windows as given by the real integrand of the reaction rate formula (solid line; see Equation 2.2). Shown in a dot-dash line on the same figure is the product of the high-energy tail of the Maxwell-Boltzmann distribution with the simple Coulomb barrier penetration factor (denoted as “ $\exp(-E/kT - b/\text{sqrt}(E))$ ”); see Equation 2.4). In addition, a Gaussian approximation (“Gauss approx”) is shown with a dotted line. The Gaussian approximation is widely used to estimate the Gamow window but predicts it at too high an energy, especially for the capture reaction. For purposes of

illustration, all curves were renormalized to the arbitrary unit scale shown; for  $T_9 = 5$  all three quantities peak at 10, for  $T_9 = 2$  they peak at 6. The stars denote the energy values at which experimental data were measured from Sonzogni et al. [16] ( $^{44}\text{Ti}(\alpha, p)^{47}\text{V}$ ) and Hoffmann et al. [3] ( $^{40}\text{Ca}(\alpha, \gamma)^{44}\text{Ti}$ ). The effective temperature range for the synthesis of  $^{44}\text{Ti}$  is  $2.0 \leq T_9 \leq 4.0$ . This corresponds to a center-of-mass energy range of  $E_{c.m.} = 2.1 - 6.1$  MeV. The present work studies resonance states well within this temperature range (see Section 1.4).

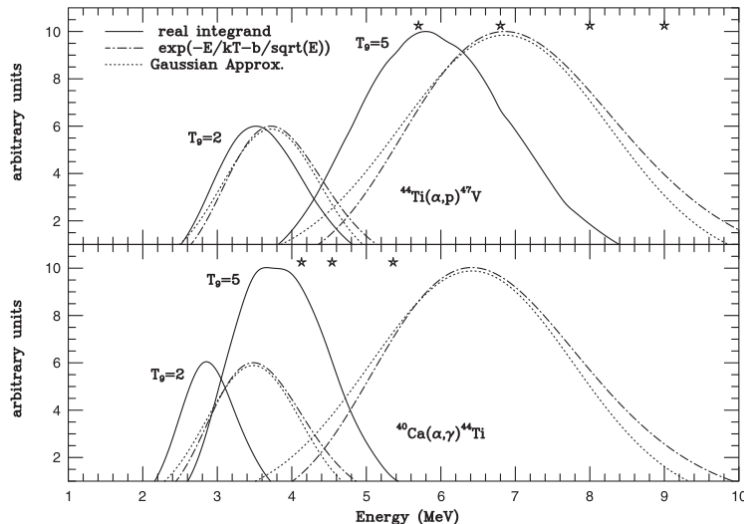


Figure 2.1: Effective Gamow windows for  $^{44}\text{Ti}(\alpha, p)^{47}\text{V}$  and the competing  $^{40}\text{Ca}(\alpha, \gamma)^{44}\text{Ti}$  reaction at  $T_9 = 2$  and  $T_9 = 5$ . Shown are the true Gamow windows as given by the real integrand of the reaction rate formula (solid line; see Equation 2.2), the product of the high-energy tail of the Maxwell–Boltzmann distribution with the simple Coulomb barrier penetration factor (denoted as “ $\exp(-E/kT - b/\sqrt{E})$ ”, dot-dash line; see Equation 2.4) and the Gaussian approximation (“Gauss approx.,” dotted line). Stars denote the energy values at which experimental data were measured from Hoffmann et al. [3] ( $^{40}\text{Ca}(\alpha, \gamma)^{44}\text{Ti}$ ) and from Sonzogni et al. [16] ( $^{44}\text{Ti}(\alpha, p)^{47}\text{V}$ ). The figure taken from Ref. [3].

## 2.3 Statistical models

### 2.3.1 Compound nucleus model

The term ‘compound nucleus’ arises from a type of nuclear reaction in which a projectile is absorbed in the target with which it then shares all its energy to form a compound system. In such a process, the formation and the decay of the compound nucleus are independent. In other words, a compound system loses the memory of the way it was created. This compound nucleus amnesia hypothesis was developed by Niels Bohr [28] and is written in

terms of reaction cross sections as [27]:

$$\sigma_{X(a,b)Y} = \sum \sigma_{aX}^{CN} \frac{\Gamma_{bY}}{\sum_{chan} \Gamma_{chan}}. \quad (2.7)$$

In this equation, the reaction  $X(a, b)Y$  cross section corresponding to the decay in channel  $b$  from the compound nucleus formed in the entrance channel  $a$ , is given by the product of the compound nucleus formation cross section  $\sigma_{aX}^{CN}$  at a given energy, spin and parity by the probability to decay in channel  $b$  given all open channels  $chan$ . In the compound nucleus model, the decay in a given outgoing channel

$$\frac{\Gamma_{bY}}{\sum_{chan} \Gamma_{chan}} \quad (2.8)$$

depends on the ratio of the probability to decay in this specific channel with respect to all possible decay probabilities.  $\Gamma$  is the width of a nuclear state whose decay time is given by

$$\Delta t \sim \hbar/\Gamma_{bY}, \quad (2.9)$$

in accordance with the Heisenberg relation :

$$\Delta E \Delta t \sim \hbar. \quad (2.10)$$

### 2.3.2 Hauser-Feshbach model

As discussed above, a compound nucleus can be described in two separate parts; its formation and its subsequent decay. The Hauser-Feshbach model builds on these foundations [18]. At high excitation energies the resonances ( $\Gamma$ ) in the compound nucleus become broader and overlap. The levels overlap considerably such that little structure remains in the cross section. The cross section varies smoothly with energy and its properties can be averaged over the resonance structure. From this, Equation 2.8 can be approximated as [27]:

$$\frac{\Gamma_{bY}}{\sum_{chan} \Gamma_{chan}} = \frac{T_{bY}}{\sum_{chan} T_{chan}} \quad (2.11)$$

where  $T$  are the transmission coefficients corresponding to the decay probabilities. With the addition of angular momentum  $J$  in the compound nucleus formalism, the HF model is then given by

$$\sigma_{X(a,b)Y}^{HF} = \sum \sigma_{aX}^{CN} \frac{T_{bY}}{\sum_{chan} T_{chan}}, \quad (2.12)$$

where  $\sigma_{aX}^{CN}$  is written as

$$\sigma_{aX}^{CN} = \pi \left( \frac{\lambda}{\pi} \right)^2 \frac{2J+1}{(2J_a+1)(2J_X+1)} W_{ab} T_{aX}, \quad (2.13)$$

where  $\lambda = h/\sqrt{2\mu E}$  is the deBroglie wavelength (size) of the projectile  $a$ .  $W_{ab}$  is called the width fluctuation correction factor. The correction factor enters the formalism to account for deviations from the independence hypothesis. In this regard, it enhances the elastic

channel and decrease the other competing channels at low energies or in situations when the number of competing channels is low.

The basic elements to calculating the Hauser-Feshbach cross section are: the transmission coefficient for the entrance channel ( $T_{aX}$ ) which can be obtained from an optical potential or  $\gamma$ -strength function in the case of photon induced reactions. The transmission coefficient for all exit channels ( $T_{bY}$ ). And last but not least, the number of available levels (and their energies) for all exit channels which may be obtained from level density models. In Section 1.3.3 it was mentioned that, generally for a HF model to give a reliable prediction of a reaction rate, the average level spacing,  $D$  has to be smaller than, or similar to, the average resonance width,  $\langle \Gamma \rangle$  (see Equation 1.1). In this light, one of the most important ingredients of the HF model are level densities. When the HF model is applied to a compound nucleus where the level density is not sufficiently large, the statistical model results in a misestimation of the actual reaction cross-section and therefore, reaction rate. The following section discusses level densities.

### 2.3.3 Nuclear level densities

When the compound system energy is high enough, the system may decay by the emission of a photon or a particle in the level continuum of the compound nucleus. A nuclear level density ( $\rho(E, J, \pi)$ ) has to be introduced and the transmission coefficients entering the HF equation are given by the integral [29]:

$$T(E, J, \pi) = \sum_{v=0}^{v_{bY}} T(E, J, \pi, E_{bY}^{v_{bY}}, J_{bY}^{v_{bY}}, \pi_{bY}^{v_{bY}}) + \int_{E_{bY}}^E \sum_{J_{bY}, \pi_{bY}} T(E, J, \pi, E_{bY}, J_{bY}, \pi_{bY}) \cdot \rho(E_{bY}, J_{bY}, \pi_{bY}) dE_{bY}. \quad (2.14)$$

In this equation, the variables  $(E, J, \pi)$  correspond to the excitation energy  $E$ , spin  $J$  and parity  $\pi$  of the excited states in the compound nucleus. The variables  $(E_{bY}, J_{bY}, \pi_{bY})$  correspond to the excitation energy  $E$ , spin  $J$  and parity  $\pi$  of the channel bY. In the Hauser-Feshbach formalism, reasonable input choices for nuclear level densities can lead to significant variation in the cross sections and reaction rates.

Nuclear level densities (NLDs),  $\rho(E, J, \pi)$  have been widely studied for decades. In this section, a summary of the main qualitative features are presented. NLDs are defined as the number of nuclear levels per MeV around an excitation energy  $E$ , for a certain spin  $J$  and parity  $\pi$ . NLDs are an important ingredient to the statistical HF model. In such a statistical model, nuclear level densities are used at excitation energies where discrete level information is not available or incomplete. An important aspect of level densities is that they characterize the excitation structure of compound nuclei and have its global behaviour as a function of excitation energy. Experimentally, for low-lying excitation energies, level

densities are extracted often by directly counting of the observed levels. Experimental data suggests an exponential increase of the cumulated number of discrete levels  $N(E)$  with energy. This leads to an expression of level density for energies less than  $E$  [30]:

$$\rho(E) = \frac{dN(E)}{dE} \quad (2.15)$$

with the nuclear level cumulatives  $N(E)$  given by

$$N(E) = \int_E^{E+\Delta E} \rho(E', J, \pi) dE'. \quad (2.16)$$

In theory, level density models come in two categories; phenomenological effective models and microscopic models. Phenomenological effective level density models are based on empirical observations and a proper choice of the energy-dependent level density parameter values. The various different phenomenological models are the constant-temperature, Fermi gas model, the back-shifted Fermi gas model, and the generalised superfluid model. These models are detailed in Ref. [31] and the references therein. For the purpose of this work, the focus will be on the microscopic approaches known as Hartree-Fock-Models, in particular the Hartree-Fock-Bogolyubov (HFB) description due to its detailed information about nuclear energy levels, masses, spin and parity into the calculation of the level density.

The HFB (Skyrme force) from Hilaire's combinatorial tables [32] is the microscopic nuclear model used to calculate level densities in this work. The model evaluates particle-hole level densities as a function of energy, spin and parity, taking the collective behaviour of nuclei such as rotation and vibration into account. These HFB calculations within the Skyrme framework are performed using an effective interaction adjusted for nuclear masses and nuclear matter properties. This microscopic approach is based on a consistent treatment of shell effects, pairing correlations, deformation effects and collective excitations in both spherical and deformed nuclei. HFB plus combinatorial model level densities for more than 8500 nuclei are catalogued and made available in tabular format, for excitation energies up to 200 MeV and for spin values up to  $J = 49$  in the online Reference Input Parameter Library (RIPL-3) [33]. These calculated level densities are compared to the experimental results by inspection of the cumulative distributions  $N(E)$ .

## Chapter 3

# Experimental setup

### 3.1 Introduction

The  $^{50}\text{Cr}(p,t)^{48}\text{Cr}$  experiment discussed in this dissertation is the first to resolve and provide precise excitation energies of the  $\alpha$ -unbound states in the region of astrophysical interest (9 to 14 MeV in excitation energy). The use of forward-angle, high resolution (p,t) measurements to investigate possible ( $\alpha$ ,p) resonances in isospin  $T_z = (-1,0,1)$  nuclei using the K600 magnetic spectrometer came after the development of the high energy-resolution  $0^\circ$  facility used to perform such (p,t) reaction measurements at iThemba LABS [25]. In the past, the  $0^\circ$  setup has been utilised successfully to study the natural parity resonances in  $^{38}\text{Ca}$  [23] and  $^{22}\text{Mg}$  [24].

A brief overview of the iThemba LABS facility which houses the Separated Sector Cyclotron (SSC) and other accelerators which were used in this study to deliver a proton beam of 100 MeV to the K600 spectrometer is presented in this chapter. The beam was then transported through a set of magnetic components along the beam line to the scattering chamber at the target position of the K600 magnetic spectrometer. A description of the spectrometer and its settings during the experiment will also be presented along with the focal-plane detector system and the associated data-acquisition system.

### 3.2 The iThemba LABS accelerator facility

iThemba LABS is a multidisciplinary institution with interests ranging from nuclear physics research to nuclear medicine [34]. The main accelerator building floor plan is shown in Figure 3.1. It hosts 3 accelerators: the smaller pre-accelerator Solid Pole Cyclotrons (a K8 SPC1 and a K11 SPC2) and a K200 Separated Sector Cyclotron (SSC). In a classical picture, cyclotrons are made up of 2 semi-circular capacitive electrodes called “dees” under a homogeneous magnetic field,  $B$ , and constant revolution time which are used to accelerate

charged particles. The K-value in the name of a cyclotron (e.g. K200) is the kinetic energy reach for protons from bending strength in non-relativistic approximation:

$$K = \frac{e^2}{2m_p}(B\rho)^2, \quad (3.1)$$

where  $m_p$  is the mass of a proton in amu,  $e$  is the electric charge and  $\rho$  is the gyroradius. K is given in MeV. The SSC can accelerate protons up to an energy of 200 MeV. K can be used to rescale the energy reach of protons to other charge-to-mass ratios:

$$E = K \frac{Q^2}{A}, \quad (3.2)$$

where  $Q$  and  $A$  are the charge state and mass number of the accelerated charged particle, respectively.

During the experiment, a proton beam was produced from hydrogen gas in an Electron Cyclotron Resonance (ECR) ion source and pre-accelerated by SPC2. To obtain the requisite proton beam energy of 100 MeV for this experiment, the proton beam coming from the SPC2 was injected via the K-beam line into the K200 SSC (see Figure 3.1). The acceleration of the beam is made possible by the SSC's characteristic radio frequency (RF) which is used as a rapidly alternating electric potential applied to its dees in order to change the direction of the field which enables the acceleration. To be able to obtain a cleaner focal plane particle identification, the accelerator system pulse selector was used. The pulse selector is an RF component located before the K200 cyclotron which deflects a portion of the beam pulses. A pulse selection of 1 in 6 was used for this experiment. This means that only 1 in every 6 beam pulses was allowed to travel down the beamline and impinge upon the target.

After attaining an energy of 100 MeV from the SSC, the pulsed beam is extracted into the X-line. Once exiting the X-line, the beam moves to the P-line using the bending magnet, B1P, before reaching a second bending magnet, B3P, to enter the S-line that leads to the K600 spectrometer.

### 3.3 Scattering chamber

After moving into the S-line, the beam enters the small-angle mode scattering chamber (see Figure 3.2) just before it reaches the spectrometer. This scattering chamber was designed with the intention of having a silicon-detector array, the CAKE [36] placed inside it. Inside the chamber is a target ladder on which a number of targets were mounted. The ladder can hold up to six targets at a time. The targets (listed in Table 3.1) used during the experiment in question, were either for diagnostic purposes, calibration or as targets to investigate the states of interest.

A 1.052 mg/cm<sup>2</sup> <sup>12</sup>C target was used to check that the K600 is working properly. It was also used to calibrate the reaction product scattering angles via an elastic scattering

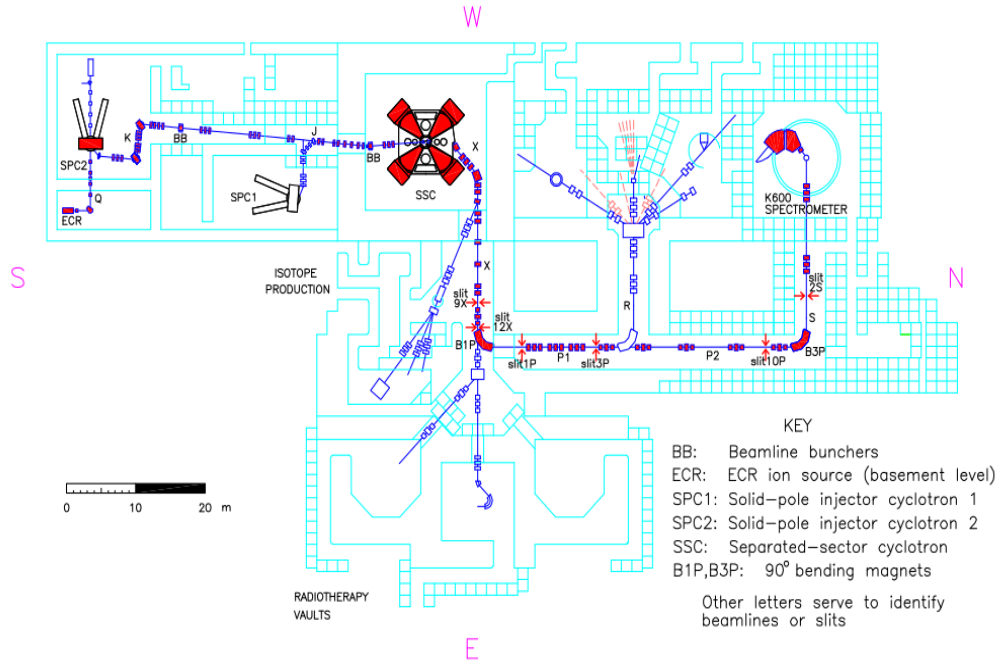


Figure 3.1: Layout of the iThemba LABS SSC facility [35].

reaction and to identify possible contamination peaks coming from the carbon-backed  $^{50}\text{Cr}$  target. A  $0.2 \text{ mg/cm}^2$  Mylar ( $\text{C}_{10}\text{H}_8\text{O}_4$ ) target was used to identify possible contaminant peaks in the focal plane coming from  $^{14}\text{O}$  and  $^{10}\text{C}$ . A  $0.7 \text{ mg/cm}^2$   $^{24}\text{Mg}$  target was used for magnetic rigidity calibration of the focal plane. Finally, a  $1.15 \text{ mg/cm}^2$  carbon-backed  $^{50}\text{Cr}$  target was used to populated states in  $^{48}\text{Cr}$  ( $0.75 \text{ mg/cm}^2$   $^{50}\text{Cr}$  evaporated onto a  $0.4 \text{ mg/cm}^2$   $^{12}\text{C}$  backing). Such a target contains 2 main sources of contamination: the carbon from the target backing and the oxygen that gets infused into the target during the  $^{50}\text{Cr}$  deposition process.

Table 3.1: List of targets used the experiment and their purposes.

Target	Thickness( $\text{mg/cm}^2$ )	Purpose
carbon-backed $^{50}\text{Cr}$	1.15	Primary target
$^{12}\text{C}$	1.052	Diagnostics, scattering angle calibration and background
Mylar ( $\text{C}_{10}\text{H}_8\text{O}_4$ )	0.2	Background
$^{24}\text{Mg}$	0.7	Focal plane calibration

The scattering chamber is connected by a flange to the collimator which allows ejectiles within a scattering angle of  $\pm 2^\circ$  into the K600. The charged particles that are permitted to enter the spectrometer aperture were momentum analysed by the K600 magnetic spectrometer and observed in the focal plane detection system, giving us precise energy information

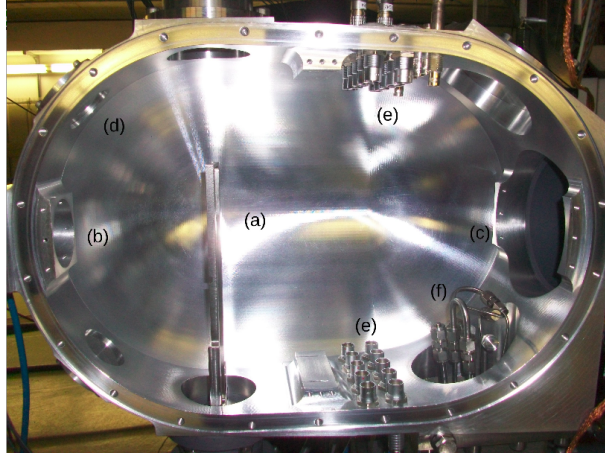


Figure 3.2: Picture showing a transverse view of the new small angle scattering chamber [24]. The beam direction is from left to right. (a) The target ladder, (b) beam entrance, (c) beam exit, (d) window to view the targets, (e) feedthrough connectors for the CAKE, (f) inlets/outlet pipes that can be used to channel gases/liquids into or out of the chamber.

on excited states populated in  $^{48}\text{Cr}$ .

### 3.4 The K600 magnetic spectrometer

The K600 magnetic spectrometer at iThemba LABS is a high-resolution spectrometer used to momentum analyse ejectiles coming from nuclear reactions. This particular magnetic spectrometer can bend protons and  $\alpha$ -particles of up to 600 MeV and tritons up to 200 MeV (see Equation 3.2). The spectrometer can be set up to perform measurements at different lab angles including at  $0^\circ$ . Figure 3.3 shows a diagram of the spectrometer at a  $0^\circ$  configuration. The function of the spectrometer is to momentum analyse scattered particles, with the primary detection principle of the spectrometer based on the concept of magnetic rigidity. Throughout the text, magnetic rigidity is given in its non-relativistic form:

$$B\rho = \frac{mv}{q} = \frac{p}{q} \quad (3.3)$$

where  $B$  is the magnetic field,  $p$  is the linear momentum of the ejectile and  $\rho$  is the gyroradius. The ion-optics of the spectrometer governed by Equation 3.3, imply that the focal plane position  $\rho$  can be interpreted directly in terms of linear momentum,  $p$ , for scattered particles of the same charge. The focal-plane position ( $\rho$ ) of the ejectiles is thus important for this experiment as it allows for an easy conversion between position and momentum; giving, through reaction kinematics, the excitation energy of the recoil nucleus. Experimentally,  $\rho$  is determined by way of multi-wire drift chambers (see Section 3.5).

In this experiment, tritons corresponding to  $^{48}\text{Cr}$  excitation energies ranging from 9 to 14 MeV were observed on the focal plane. With this reaction,  $^{50}\text{Cr}(p,t)^{48}\text{C}$ , occurring at

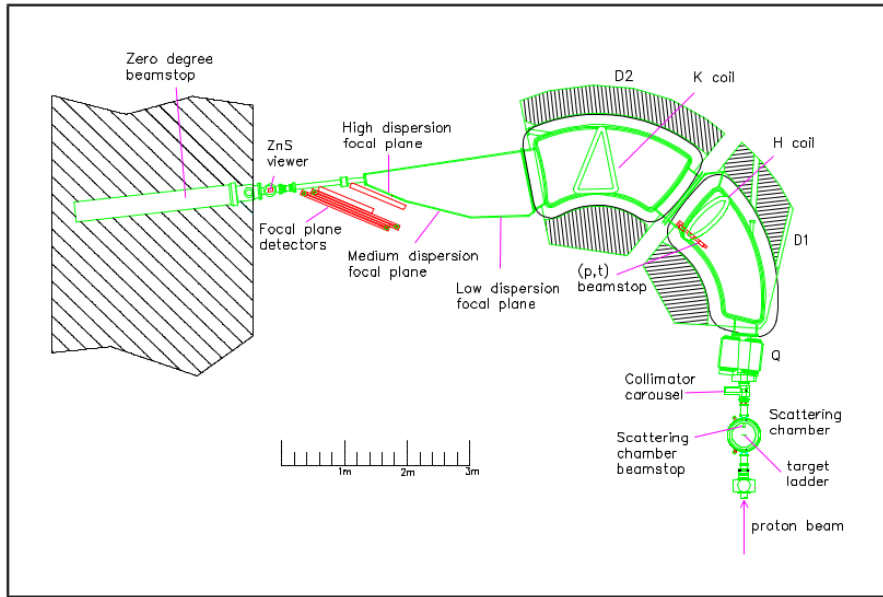


Figure 3.3: A diagram of the K600 spectrometer at  $0^\circ$  [35]. Note: The focal plane detectors were placed at the medium dispersion focal plane and the collimator carousel was not in place for this experiment.

the beam energy of 100 MeV and at a lab angle of  $0^\circ$ , the triton energy range of interest is 70 to 75 MeV. The program TRACK v8.6 [37] was used to calculate the trajectory of the corresponding unreacted proton beam and tritons, taking into account excitation energies needed for calibration and their placement on the focal-plane. Figure 3.4 shows a TRACK trajectory simulation with the trajectories of the minimum and maximum energy of tritons from the  $^{50}\text{Cr}(p,t)^{48}\text{Cr}$  reaction with energies 69 MeV and 78 MeV, respectively.

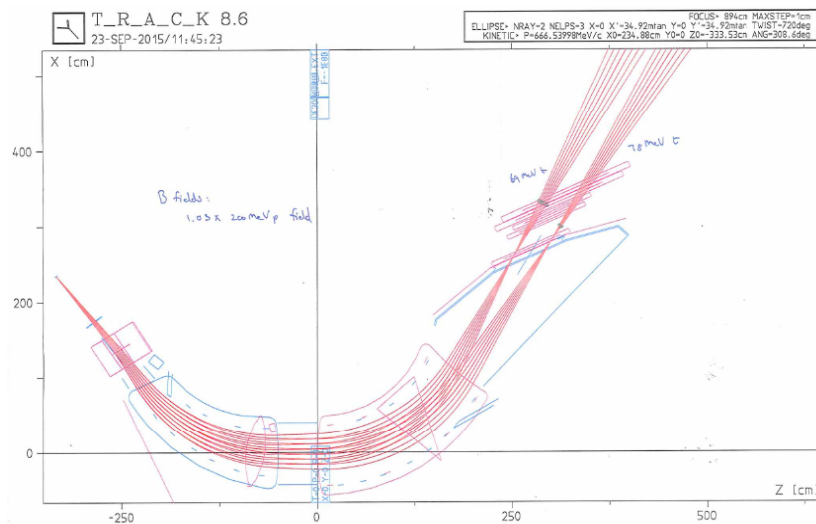


Figure 3.4: TRACK v8.6 simulated triton trajectories following the  $^{50}\text{Cr}(p,t)^{48}\text{Cr}$  reaction. Image taken from Ref. [38].

From these calculations, the beamstop position was also determined. The beam stop, a brass block (see Figure 3.5), was placed inside the first dipole magnet. An accurate indication of the position of the beamstop is important because if it is misplaced, the unreacted beam would cause a large amount of unwanted reactions within the spectrometer and the focal-plane detector.



Figure 3.5: The (p,t) beamstop. Note that it consists of two separate brass blocks, each with dimensions 70 mm (deep) x 55.5 mm (wide) x 55 mm (high). These dimensions includes the lip, which is 5 mm wide and 10 mm deep.

The ejectiles emerging from the scattering chamber enter the K600 at the first active element of the spectrometer, the vertically focusing quadrupole magnet. This component ensures the transmission of the ejectiles through the spectrometer. Four other elements are encountered along the way. The momentum dispersion of ejectiles is controlled by dipole elements, D1 and D2. The ratio, R is given by:

$$R = \frac{B(D1)}{B(D2)} \quad (3.4)$$

where  $B(D1)$  and  $B(D2)$  are the magnetic field magnitude of the 1st and 2nd dipole of the K600, respectively. The ratio gives the choice of high-/medium-/low-dispersion focal planes according to the kinematics and the energy resolution required for the experiment. These focal-planes are situated after the second dipole (D2) (see Figure 3.3). The medium-dispersion focal plane was used for this experiment. The technical specifications of the spectrometer for use at the medium dispersion focal plane are reported in Table 3.2.

The other 2 elements are the 2 higher multipole coils (H- and K-coil). The K-coil, a pole face current winding which introduces both a dipole and quadropole component, is used to adjust for first-order kinematic variations of momentum with angle of the form  $(x|\theta)$ . The H-coil, a pole face current winding which introduces both a dipole and hexapole component, is used to correct for  $(x|\theta^2)$  aberrations.

Table 3.2: The calculated ion-optic matrix elements of the K600 magnetic spectrometer for the medium-dispersion focal plane [39].

Matrix element/ characteristics	Medium dispersion R = 1.00
$(x x)$	-0.52
$(\theta \theta)$	-1.89
$(y y)$	-5.45
$(\phi \phi)$	-0.20
$(x \frac{\Delta p}{p})$	-8.4 cm/%
$P_{max}/P_{min}$	1.097

## 3.5 Focal-plane detectors

The task of the focal-plane detector system is to detect the position (to get excitation energy) and to identify particles by providing timing, energy loss, position and angular information of the ejectile at the focal plane. The K600 magnetic spectrometer focal plane detector system consists of up to two wire-chambers and up to two plastic scintillators. For this experiment, the detectors were ordered as follows: the XU VDC detector (VDC1), the X detector (VDC2), a 6.35 mm plastic scintillator (Paddle 1) and lastly, a 12.5 mm plastic scintillator (Paddle 2). The two wire-chambers provide position and, when combined, angular information about the ejectile while the two plastic scintillators yield timing and energy loss information to perform particle identification. Details about the detection systems follows below.

### 3.5.1 Vertical Drift Chambers

Data of the respective positions and scattering angle of the ejectiles on the focal plane were recorded by the vertical drift chambers. The position at which the incoming ejectile hits the wires and the scattering angle is obtained from the reconstruction of the ejectile tracks within the focal plane. To obtain the reconstruction of the ejectile tracks, an XU signal wire configuration found in the new VDC of the drift chamber was used along with X only signal wire old VDC, leading to an overall XUX multi-wire drift chamber configuration. Figure 3.6 shows a computer generated picture of the XU VDC detector. In these drift chambers, the X signal-wires are perpendicular to the scattering plane i.e. vertical, while the U signal-wires are angled at  $50^\circ$  in relation to the scattering plane.

The X-wire-planes in both the old and new VDCs are lined with 198 gold-plated tungsten signal wires placed 4 mm apart. Each wire has a diameter of  $20 \mu\text{m}$ . Interspersed between these wires are 199 gold plated tungsten field-shaping wires. These wires are thicker ( $50 \mu\text{m}$



for each wireplane is defined as:

$$\text{Efficiency} = \frac{\text{Number of accepted events}}{\text{Total number of events}} \quad (3.5)$$

The conditions for accepted VDC events are that a minimum of 3 and a maximum of 8 wires must be activated. Within a group of activated wires, no wires can be separated by more than 3 inactive signal wires. Each of the activated wires must yield a drift time within the valid mapping region. The efficiencies of the VDC wire planes for the chained  $^{50}\text{Cr}(\text{p,t})^{48}\text{Cr}$  runs are tabulated in Table 3.3.

For the specific drift chamber used, drift distances of 8 mm can be expected corresponding to drift velocities and times of the order  $4\text{-}6 \times 10^4$  m/s and 133-200 ns, respectively [40]. Thus, by making use of this drift time to drift distance mapping, together with the measurement of the time taken for electrons to drift from the primary point of ionization to the point where avalanching occurs, it is possible to accurately reconstruct the particle position on the focal plane. A detailed explanation of timing to position conversion is given in section 4.2.

Table 3.3: Efficiencies of the VDC wire planes for the chained  $^{50}\text{Cr}(\text{p,t})^{48}\text{Cr}$  runs.

VDC wire plane	Efficiency [%]
X1	98.4
U1	96.4
X2	98.5
Total	93.4

### 3.5.2 Plastic Scintillators

The plastic scintillator paddles were used to generate the experimental trigger for data collection and to measure of the energy loss experienced by the ejectiles. The paddles are a BC-408 type plastic scintillator [41]. BC-408 scintillators have a large area, they are suitable for time-of-flight (TOF) measurements and are used to detect charged particles, such as protons, tritons and  $\alpha$ -particles. The two rectangular plastic scintillator detectors were, respectively, 12.7 and 6.35 mm thick and covered an area of  $1219 \times 102$  mm<sup>2</sup>. Coupled on both ends of the paddles, via light guides, are photo-multiplier tubes (PMTs) which are operated in coincidence mode. The PMTs are Hamamatsu R329-02 PMT tube [42], coupled with a Hamamatsu E934 base. The timing resolution of the PMT, (i.e. anode pulser rise time) is about 8-9 ns. The gain is a function of the voltage supplied to the PMT. Aluminized Mylar sheeting was used to isolate the paddles from the environment.

Coincidence signals from these PMTs are used for particle identification and the generation of fast timing signals which provide trigger signals for the Data Acquisition (DAQ)

system. Due to the outgoing energies of the triton ejectiles, most reaction products are stopped within millimeters in paddle 1, with only a few high energy tritons reaching the second scintillator. The energy deposited in the scintillator depends on the type of particle and the kinetic energy of the particle. With aid from the time-of-flight measurements together with energy loss particle identification (PID) spectra, reaction products can successfully be observed.



Figure 3.8: Plastic scintillator paddles of the K600 focal plane detector system [24].

## 3.6 Electronics and DAQ

The DAQ for this experiment was carried out over 3 weekends; 01-04, 08-11 and 16-18 October 2015. The total beamtime is tabulated in Table 3.4. The DAQ involved the merging of the MIDAS data acquisition system (MIDAS DAQ) [43] with the Versa Modula Europa (VME) based DAQ of the K600.

Table 3.4: Beamtime tally on targets used during the experiment.

Target	Beam Time [hr:min:s]
$^{50}\text{Cr}$	23:13:2
$^{12}\text{C}$	3:9:29
Mylar	3:54:34
$^{24}\text{Mg}$	6:17:21

### 3.6.1 Trigger logic

Figure 3.9 shows a flow chart of the trigger electronics used in this work. For this experiment, a single paddle trigger was used. Two PMTs attached on either end of the paddle, provided the signals for the trigger electronics. The signal provided by each PMT was sent to a



system busy signal from the QDC to create the inhibited count. The system dead time could be determined by comparing the number of pulses measured by the two scaler modules.

### **3.6.2 Pre-amplifiers and TDCs**

Signals from the VDC wire-planes are pre-amplified and sorted by Technoland PTM 005 16-channel electronic cards, which are located on the VDC PC board. The pre-amplifier cards amplify the signals from the signal wires, and perform a discriminatory function to ensure that only proper signals will be processed by the TDCs. Using 16-channel twisted-pair ribbon cables, the signals are transported to the CAEN V1190A TDCs. The TDCs store the K600 timing information and are capable of 100 ps resolution. In total, 35 pre-amplifier cards were used. 13 pre-amplifiers for the 198 signal wires of the X wire plane of VDC1, 9 pre-amplifiers for the 143 signal wires in the U-wire plane of VDC1 and lastly, 13 pre-amplifiers for the 198 signal wires for the X wire plane of VDC2. These timing signals are used for the purpose of particle identification. See Section 4.2.1 for a detailed explanation of particle identification.

### **3.6.3 DAQ**

The digitisation of the electronic signals was carried out by three Versa Modula Europa (VME) modules: VME TDCs (CAEN V1190), VME scalers (CAEN V830) and VME QDC (CAEN V792). Coupled with the VME modules is the Maximum Integrated Data Acquisition System (MIDAS), a software package that contains libraries which are used for data transport and a set of programs for recording data and system management.

# Chapter 4

## Data Analysis

### 4.1 Introduction

A 100-MeV pulsed beam of protons initiated a  $^{50}\text{Cr}(p,t)^{48}\text{Cr}$  reaction. The outgoing tritons from the reaction were momentum analysed by the K600 magnetic spectrometer. Tritons with energies ranging from 69 to 78 MeV were observed at the focal plane. This chapter outlines the analysis of these tritons to establish the excitation energies of  $^{48}\text{Cr}$ .

To begin with, it is necessary to distinguish between the triton ejectiles and other charged particles that may be detected at the focal plane. This particle identification process is outlined in section 4.2. Ejectile trajectory reconstruction follows particle identification. The reconstruction included the determination of the focal-plane positions and scattering angles associated with tritons passing through the focal-plane. Next, in section 4.3, the position information is used to establish the triton momenta and the associated excitation energies.

### 4.2 Data Extraction

#### 4.2.1 Particle Identification

Particle identification (PID) is a process of selecting focal-plane events belonging to the desired reaction channel. Following PID, we obtain the K600 data analysis optimization parameters such as the cable lengths, the look up tables (LUT) and the scattering angles for the selected particles. These optimisation parameters are used to reconstruct the focal-plane positions of the ejectiles as recorded by the VDCs. PID is carried out using time-of-flight (TOF) and energy losses of ejectiles in the plastic scintillators of the focal-plane. The TOF is measured as the relative time elapsed between a coincident scintillator signal and the next RF signal from the SSC.

Figure 4.1 shows such a TOF vs scintillator energy matrix. The spectra shows ejectiles

observed on the focal-plane during this experiment. These ejectiles are the tritons coming from the (p,t) channel (for illustrative purposes, delimited in red) and possibly deuterons coming from a (p,d) channel [24] or some other reaction channel which is not of interest for the current experiment. Because of the cleanliness of the data, only one software gate on the tritons locus was sufficient for use across all data runs. The unreacted beam of protons does not reach the focal plane, it is swept away by the magnetic fields into a beam stop located inside the first dipole magnet (D1) of the K600.

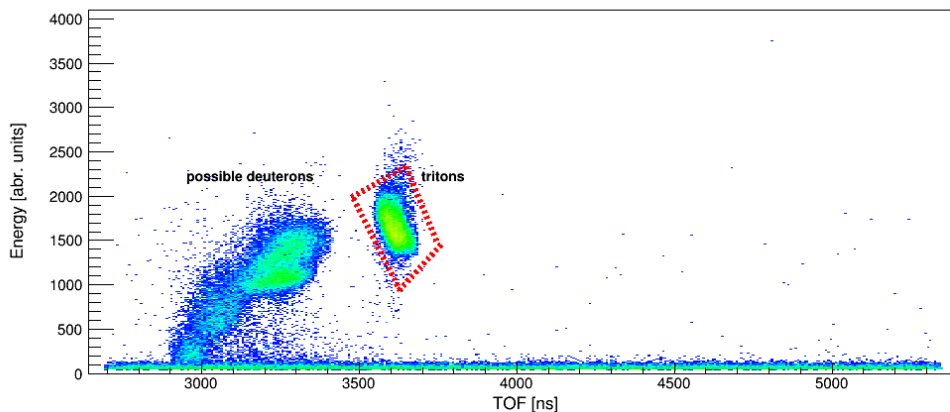


Figure 4.1: The particle identification (PID) spectrum. The tritons locus is delimited in red. The rigidity of the triton ejectiles is highest making the locus easily identifiable in the spectrum. The locus on the left of the tritons locus might be due to (p,d) reactions where the deuterons are able to reach the focal plane.

## 4.2.2 Focal-plane event reconstruction

### 4.2.2.1 Cable lengths

An important input needed to reconstruct the focal-plane positions is the time between signal creation in the VDC and signal storage. For each drift cell in the VDC the conversion of measured drift times to drift distances is achieved by a lookup table (LUT) (see LUT section below). There is only one lookup table per drift plane. Therefore one must ensure that the measured time range for the drift times of all the wires per wireplane are similar.

After a VDC wire is triggered, there is a delay between the creation of the electrical signal at the pre-amps and the arrival of this signal to the TDCs. The relative differences in the delays, by and large, are dominated by the differences in the physical cable lengths between the preamplifiers and the TDC modules. These relative delays between each of the TDC channels must be corrected to ensure accurate focal plane position calculation. The correction was done by aligning the trailing edge of the TDC channel vs TDC time 2D-spectra (see Figure 4.2).

The cable length offsets, which provide the necessary corrections, were generated using a custom in-house algorithm described in Ref. [40]. The algorithm determines the minimum gradient of the peak on the short drift time side of the drift time spectra for each individual channel, and calculates the necessary offset relative to a fixed parameter which is defined in the C++ script. Although the algorithm is automated, if a channel has low statistics, the algorithm does not provide an accurate offset. Additional manual corrections were made to the generated cable length offsets. Figures 4.2 and 4.3 show the spectra of TDC channels versus uncorrected and corrected drift times, respectively. In Figure 4.3, the spread of the drift time distributions in Figure 4.2 have been removed.

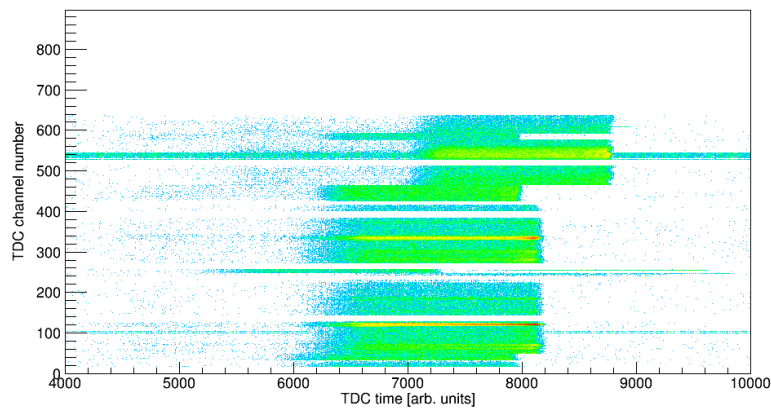


Figure 4.2: Spectrum showing the uncorrected TDC channel number versus TDC time of the VDC wires for a typical run. Note: the strong response around channel number 520 is due to wires with a lot of noise.

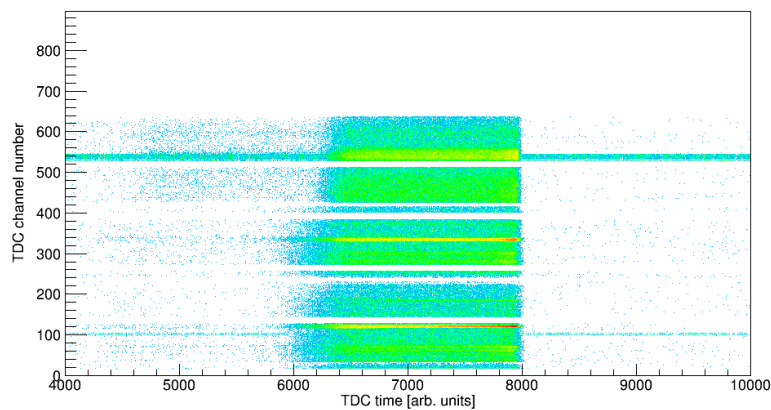


Figure 4.3: Spectrum showing the corrected TDC channel number versus TDC time of the VDC wire following the cable length corrections for a typical run. Note: the strong response around channel number 520 is due to wires with a lot of noise.

#### 4.2.2.2 LUT

Following the correction of the relative time delays between the TDC channels, a mapping of the drift time to drift distance in the VDCs was established. This mapping is called the Look Up Table (LUT). During the operation of the experiment, the drift time is measured from the triggering of a wire (after cascading event) to the beginning of the subsequent RF pulse of the cyclotron. As a result, a larger recorded drift time corresponds to a shorter physical drift time and distance. Shown in Figure 4.4 is the average timing response of all the X1 wire-plane signal wires. The flat region corresponds to electrons of constant drift velocity. The large peak to the right in the spectrum is associated with relatively short drift times of cascading events that are originating near the signal wires. Ideally, this procedure is performed using white runs (runs without strong structure). This ensures a homogenous probability distribution function of drift distances which correspond to a flat positional distribution on the focal plane which can be used to map the measured drift times to drift distances. In the case of this work, a chain of (p,t) runs was used, this is made possible by the cleanliness of the data and sufficient software gates used for the PID.

Once the characteristic drift-time distribution is known, it is possible to determine the drift distances of the electrons for each signal wire using:

$$y(t) = \left( \frac{dN}{dy} \right)^{-1} \int_{t_0}^t \frac{dN}{dt'} dt' \quad (4.1)$$

where  $t_0$  is the initial time the particle strikes the drift cell,  $t$  is the time at which the anode registers a pulse and  $dN/dt$  is drift-time distribution.  $dN/dy$  is the spatial distribution of events in the drift cell, which is assumed to be constant. From this, Equation 4.1 can be re-written as:

$$y(t) \propto \int_{t_0}^t \frac{dN}{dt'} dt' \quad (4.2)$$

From Equation 4.2 and the drift-time distribution, a LUT is generated (see Figure 4.5), where drift-distances are correlated with drift-times. The corresponding drift distance is shown in Figure 4.6.

#### 4.2.2.3 LUT offsets

The position resolution of the VDC is given by:

$$\Delta = \frac{x_{i+1} - x_{i-1}}{2 - x_i} \quad (4.3)$$

where  $x_i$  and  $x_{i+1}$  are the drift distances for consecutive wires  $i$  and  $i+1$  (see illustration in Figure 4.7). Ideally the measure of position-resolution ( $\Delta$ ) for a measurement would be zero. However, due to uncertainties in the drift-time measurements,  $\Delta$  is a uniform distribution around zero. It is nearly impossible to measure entirely accurate drift times, e.g. delays in

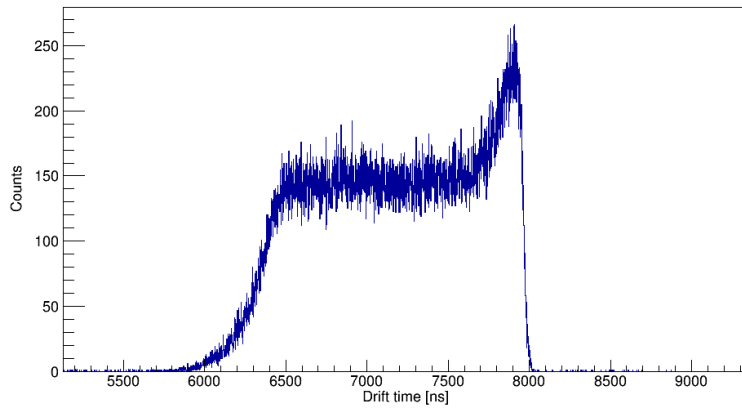


Figure 4.4: Spectrum of the drift times of the X1 wire plane.

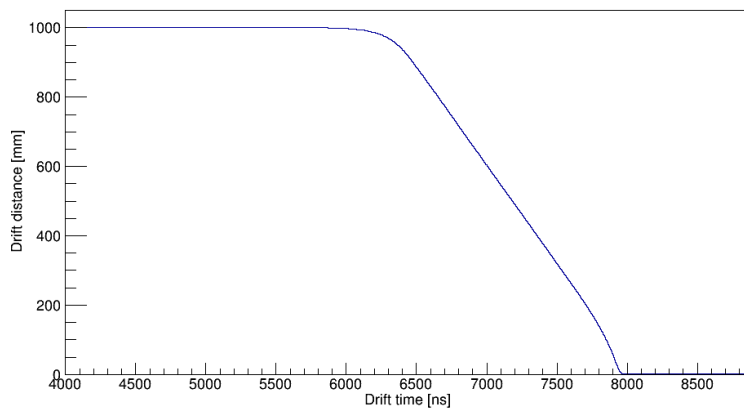


Figure 4.5: The lookup table (LUT) for the X1 wire plane.

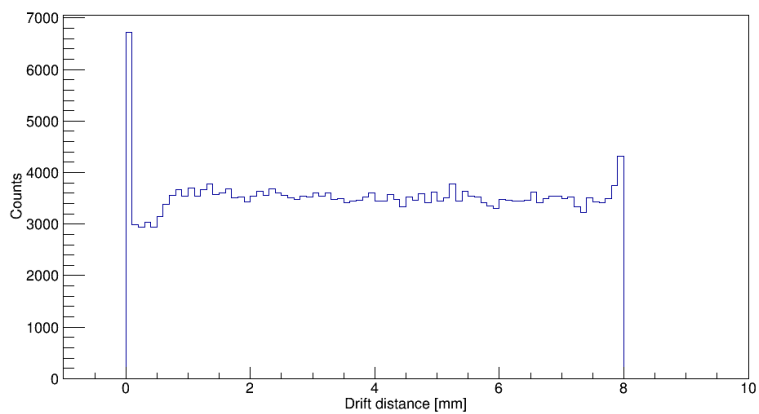


Figure 4.6: The spectrum of drift distances corresponding to the drift time spectrum in Figure 4.5.

the trigger signal commencing drift time measurements are unavoidable. Inaccurate drift times translate into poor drift distances constructed from the LUT. This results in a non-zero

offset in the LUT.

A tool to indicate whether it is necessary to correct for the offset in the LUT is a two-dimensional resolution spectrum of  $\Delta$  vs ( $\text{pos-abs}(\text{pos})$ ) (see Figure 4.8). The variable ( $\text{pos-abs}(\text{pos})$ ) is the distance between the signal wire ( $\text{abs}(\text{pos})$ ) and the calculated position at which the particle crossed the wire plane ( $\text{pos}$ ). The LUT shifts are evident in the discontinuity in the spectrum shown in Figure 4.8a. In this matrix, the straight locus above the resolution zero point corresponds to all the events below the halfway mark between two signal wires, and the straight locus below the resolution zero point corresponds to all events above the halfway mark between two signal wires. The discontinuity in the locus on the two dimensional resolution spectrum can be removed through an appropriate shift of the lookup-table (see Table 4.1 for the LUT offsets). The spectrum becomes a straight line as in Figure 4.8b, thereby optimising the VDC resolution.

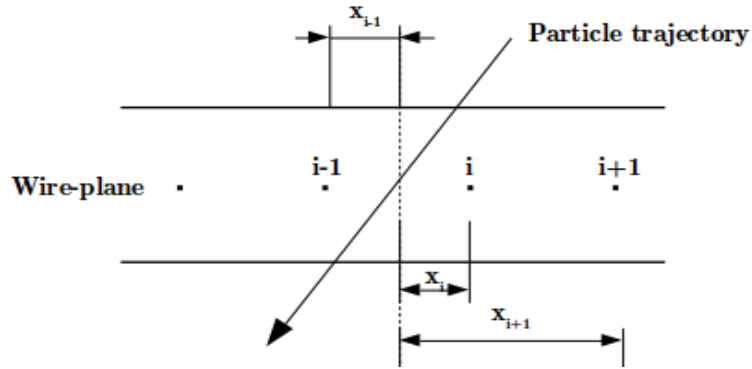


Figure 4.7: An illustration of a particle trajectory through the VDC.  $x_i$  and  $x_{i+1}$  are the drift distances for consecutive wires  $i$  and  $i+1$ .

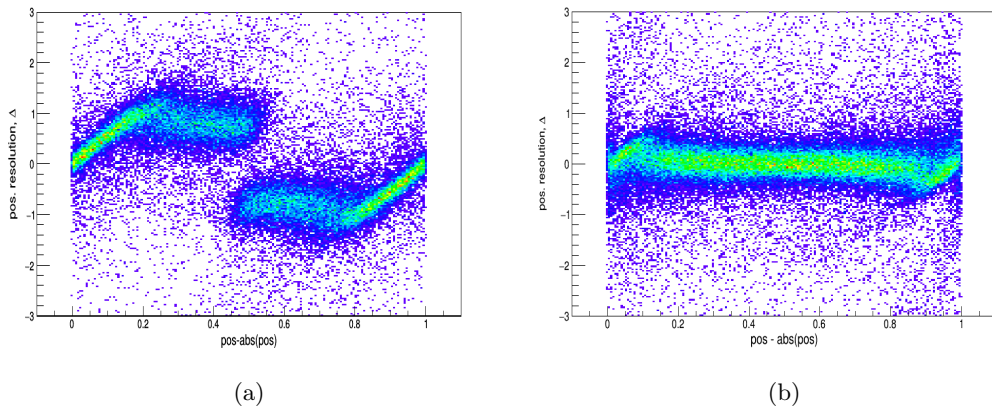


Figure 4.8: A 2D resolution plot for the X2 wire-plane. (a) Before the LUT offset was applied and (b) after LUT offset.

Table 4.1: Look up table offsets.

VDC wire-plane	offset
X1	20
U1	20
X2	15

#### 4.2.2.4 Scattering angle calibration

The objective of this experiment was to study the excitation energies of the recoil nucleus  $^{48}\text{Cr}$ . These excitation energies are not observed directly, they are calculated via two body kinematics (see Section 4.3.2). An important quantity required to obtain the excitation energies is the ejectile scattering angle ( $\theta_{SCAT}$ ).  $\theta_{SCAT}$  is the angle between the projection of the ejectile momentum vector onto the horizontal laboratory plane and the beam axis.  $\theta_{SCAT}$  is reconstructed from  $\theta_{FP}$ , the trajectory angle from the focal-plane calculated using the X1 and X2 wireplanes of the VDCs.

A series of measurements to calibrate the scattering angle were taken at a lab angle of  $4^\circ$  with a pepperpot collimator (see Figure 4.9) placed at the entrance of the K600, 862.3 mm away from the target. The holes of the pepperpot only allow ejectiles coming from fixed scattering angles to pass through to the K600. The trajectory angle from the focal-plane,  $\theta_{FP}$ , of these ejectiles is then calculated from the X1 and X2 wireplanes of the VDCs. Figures 4.10 and 4.11 shows the calculated  $\theta_{FP}$  angles at a focal-plane position of 484 mm. These plots exhibit a pattern of alternate maxima and minima for the angles for the strong state at 484 mm. The maxima correspond to the holes of the pepperpot. From this, a mapping between the fixed scattering angles of the pepperpot and the trajectory angle of the focal-plane can be created.



Figure 4.9: A picture of the pepper-pot collimator for the small angle mode. The back of the collimator, i.e. the side facing the K600, is 862.27 mm from the target. The first hole from the middle on either axis is positioned at  $0.63^\circ$ , the second hole at  $1.26^\circ$  and the third hole at  $1.79^\circ$ , spanning approximately 4.64 mrad [40].

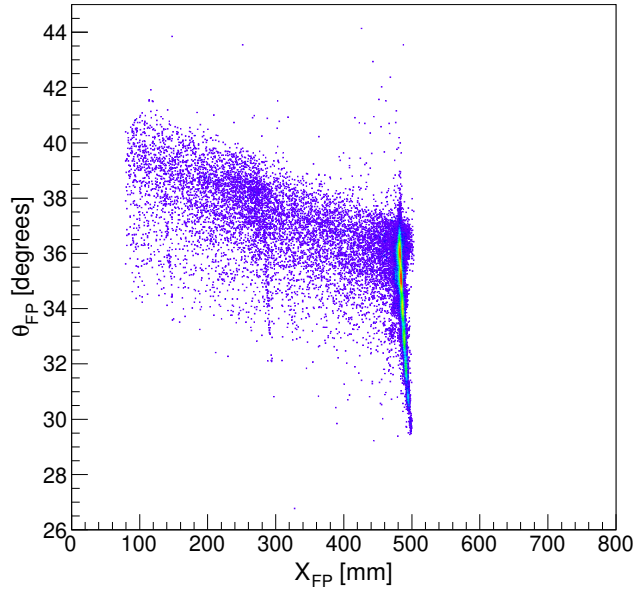


Figure 4.10: 2D Spectra showing focal-plane trajectory angle ( $\theta_{FP}$ ) versus at a focal-plane position ( $X_{FP}$ ) of 484 mm.

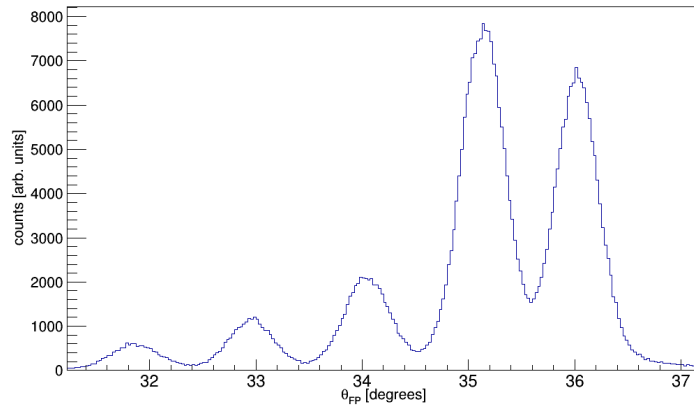


Figure 4.11: Spectra showing focal-plane trajectory angle  $\theta_{FP}$  at a focal-plane position of 484 mm.

The scattering angle calibration is given by:

$$\theta_{SCAT} = (a_1 x_{FP} + a_2) \theta_{FP} + (b_1 x_{FP} + b_2) \quad (4.4)$$

where  $a_1$ ,  $a_2$ ,  $b_1$  and  $b_2$  are the calibration parameters and  $x_{FP}$  is the focal-plane position from the X1 wire-plane. The calibration is completed in 2 steps: firstly, a mapping of the  $\theta_{FP}$  to  $\theta_{SCAT}$  is obtained for each of the focal plane positions (see Figure 4.12). Secondly, the values of the slope and offset from each of these five mappings were plotted as a function of  $x_{FP}$  (see Figure 4.13) to obtain the parameters  $a_1$  and  $a_2$ ,  $b_1$  and  $b_2$ , respectively (see Table 4.2). The reconstruction of the scattering angle ( $\theta_{SCAT}$ ) is shown in Figure 4.14.

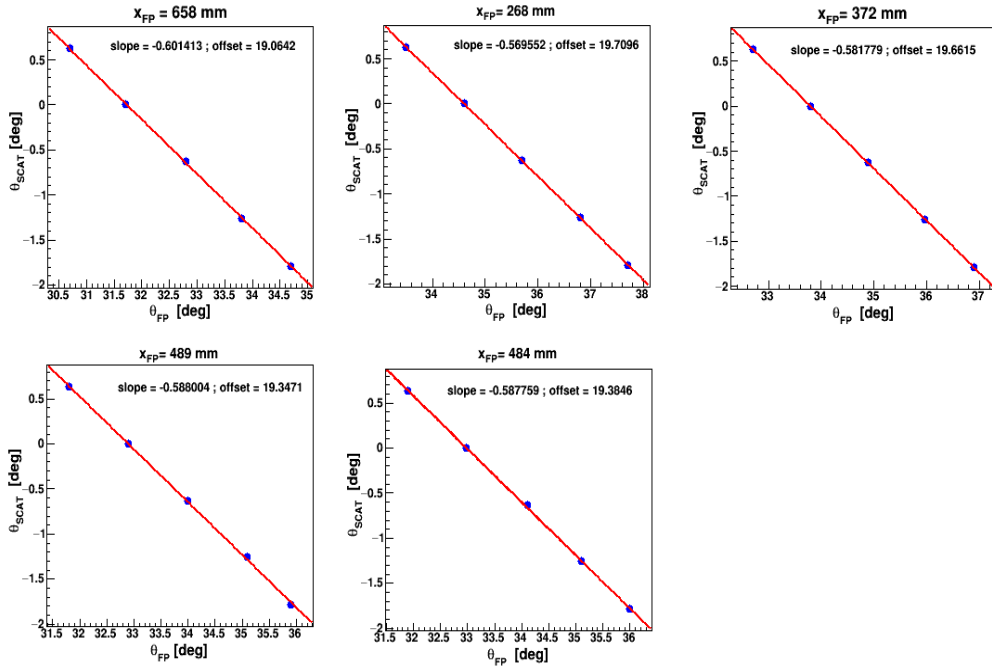


Figure 4.12: Graphs showing the mapping of focal plane angle ( $\theta_{FP}$ ) to scattering angle ( $\theta_{SCAT}$ ) at different focal plane positions ( $x_{FP}$ ).

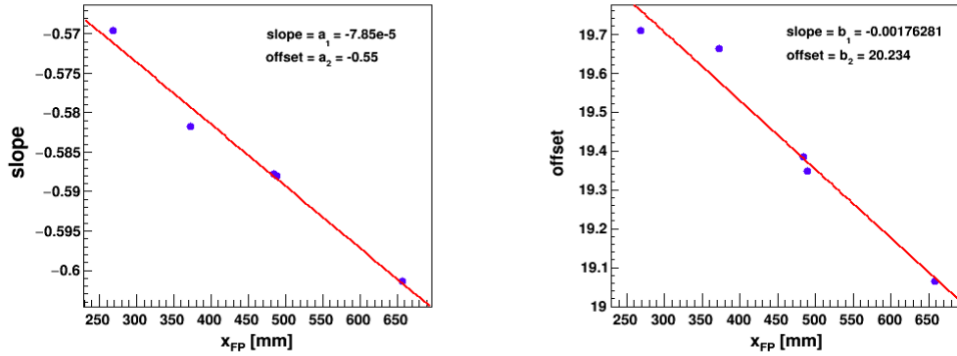


Figure 4.13: Left: The slope as a function of focal plane position. Right: The offset as a function of focal plane position.

Table 4.2: The parameters obtained for the angle calibration corresponding to equation 4.4. The uncertainty quoted are the fit uncertainties.

Parameter	Value	Uncertainty	Units
$a_1$	-0.000078	0.0000059	$\text{mm}^{-1}$
$a_2$	-0.55	0.0028	
$b_1$	-0.0018	0.000202	$\text{deg}/\text{mm}^{-1}$
$b_2$	20.23	0.096	deg

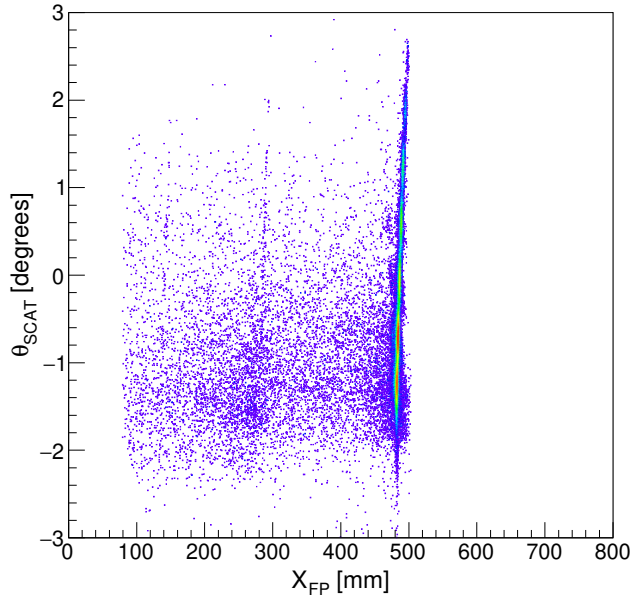


Figure 4.14: 2D Spectra showing focal-plane trajectory angle ( $\theta_{SCAT}$ ) versus at a focal-plane position ( $X_{FP}$ ) of 484 mm.

## 4.3 Data Optimisation and Calibration

### 4.3.1 Line-shape corrections

Tritons emerging from the target at the same excitation energy of the residual nucleus but at different reaction angles ( $\theta_{SCAT}$ ) have different spread in energies across the finite aperture size. This influences the resolution of states in the focal plane. Experimentally, the K- and H-coil were used to minimise this effect as mentioned in Section 3.4. However, additional corrections were required. The spectrum on the top left panel of Figure 4.15 shows the dependence of the focal-plane position on the scattering angle and the bottom left panel in the same figure shows the poor resolution of the position spectrum before the required correction.

$^{24}\text{Mg}(p,t)^{22}\text{Mg}$  data were used to perform the line shape corrections. These calibration runs have well-defined states in the focal-plane [24]. The line shape correction is achieved by ensuring that the slanted vertical lines in the  $\theta_{SCAT}$  vs focal plane position spectrum (top left panel of Figure 4.15), were corrected to be vertical (top right panel of Figure 4.15). To obtain the extent to which the line shape of a state must be corrected, point markers were placed at regular intervals along the slanted state in an attempt to reproduce the overall shape of the line, shown in Figure 4.16a. These shape marking points ( $\theta_{SCAT}, x_{FP}$ ) were fitted with a second order polynomial, given by:

$$f(\theta_{SCAT}; a, b, c) = a\theta_{SCAT}^2 + b\theta_{SCAT} + c. \quad (4.5)$$

Listed in Table 4.3 are the resulting correction parameters  $a$ ,  $b$  and  $c$ . When performing these corrections, care was taken to ensure that all the other states were not over-corrected. These software corrections were achieved by adding a value that is sensitive to  $\theta_{SCAT}$  to the original  $x_{FP}$  until the curvature is removed. The lineshape correction equation is thus:

$$x_{FP} = x'_{FP} - (a\theta_{scat}^2 + b\theta_{scat}) \quad (4.6)$$

and its application improves the resolution substantially going from a FWHM of 11.12 mm to 2.741 mm for the ground state of  $^{22}\text{Mg}$  at 601 mm, as can be observed by comparing the bottom panels of Figure 4.15.

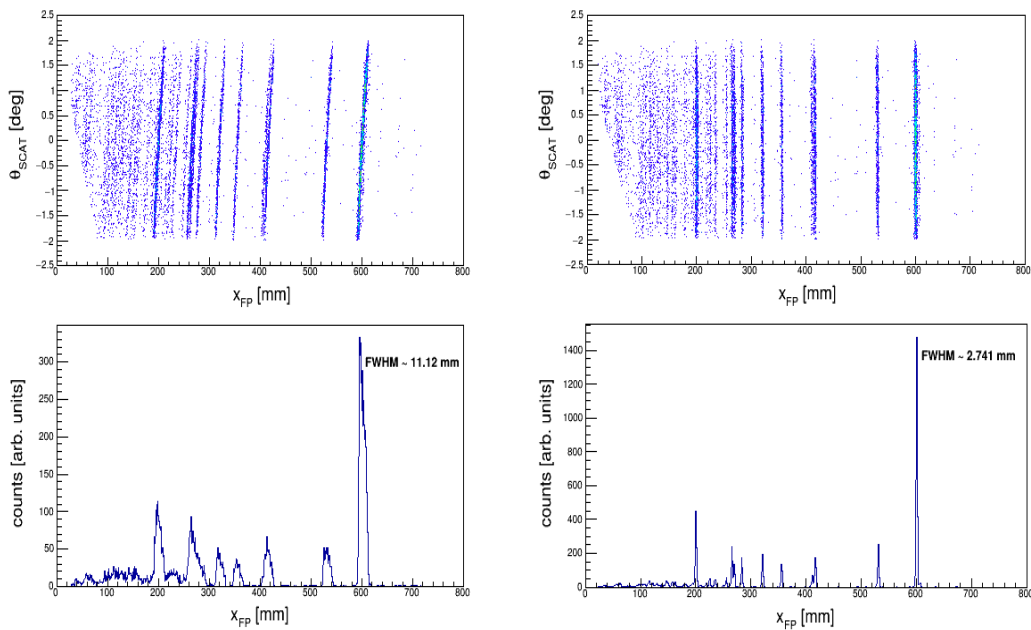


Figure 4.15: The effect of line shape correction on the  $^{22}\text{Mg}$  data. Top left panel:  $x_{FP}$  versus  $\theta_{SCAT}$  with no line shape correction applied. Top right panel:  $x_{FP}$  versus  $\theta_{SCAT}$  following line shape correction. Bottom left panel: The  $x_{FP}$  spectrum with no line shape correction applied. Bottom right: The  $x_{FP}$  spectrum following line shape correction.

The kinematics between  $^{22}\text{Mg}$  and  $^{48}\text{Cr}$  (and contaminants) are different. However, this is not a problem, the lineshape correction carried out on  $^{22}\text{Mg}$  is sufficient for the  $^{48}\text{Cr}$  data as well. Figure 4.17 shows the lineshape correction effect on the  $^{48}\text{Cr}$  data. The resolution also improves substantially going from a FWHM of 10.79 mm to 2.89 mm for the prominent  $^{10}\text{C}$  ground state contaminant situated just over 400 mm in bottom panels of Figure 4.17.

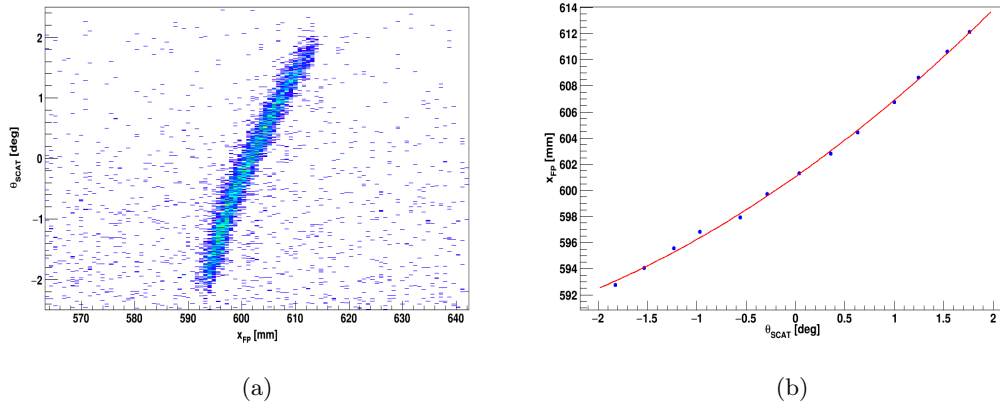


Figure 4.16: (a) The prominent ground state of  $^{22}\text{Mg}$  at 601 mm in a  $\theta_{SCAT}$  vs  $x_{FP}$  spectrum with no lineshape correction applied (b) a graph of the points used to reproduce the lineshape of the state shown in Figure 4.16a with the associated fit. The parameters of the fit are tabulated in Table 4.3.

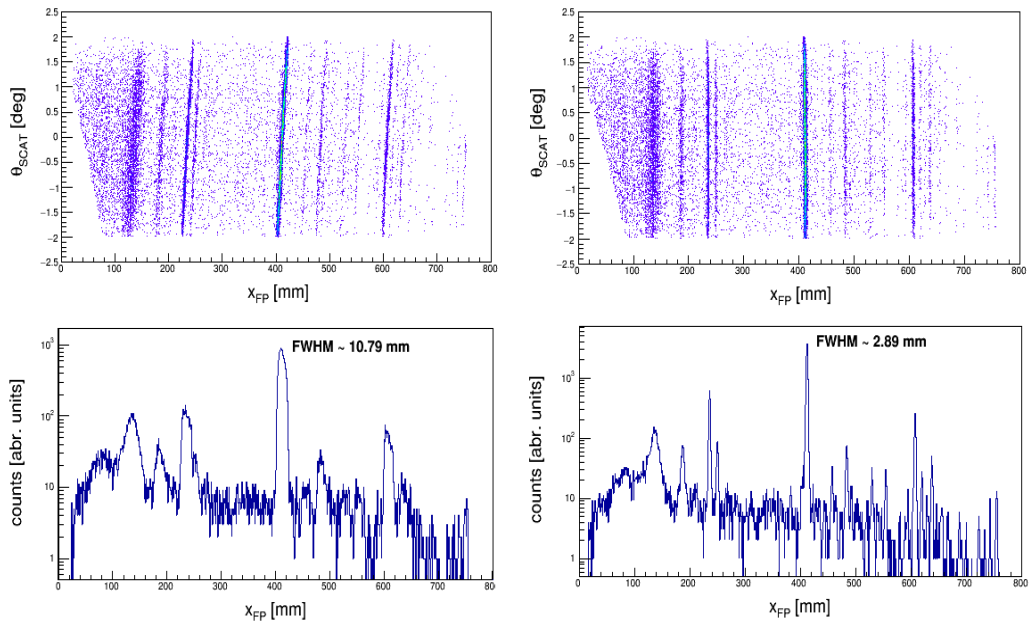


Figure 4.17: The effect of line shape correction on the  $^{48}\text{Cr}$  data. Top left panel:  $x_{FP}$  versus  $\theta_{SCAT}$  with no line shape correction applied. Top right panel:  $x_{FP}$  versus  $\theta_{SCAT}$  following line shape correction. Bottom left panel: The  $x_{FP}$  spectrum with no line shape correction applied. Bottom right: The  $x_{FP}$  spectrum following line shape correction.

### 4.3.2 Energy calibration

Energy calibration converts the focal-plane position spectrum to excitation energy. In Chapter 3, it was detailed how spectrometers are used to momentum-analyse ejectiles in order to

Table 4.3: Lineshape correction parameters for Equation 4.5.

Parameter	Value	Uncertainty	Units
a	0.53	0.063	mm/deg <sup>2</sup>
b	5.33	0.063	mm/deg
c	601.0	0.11	mm

relate a physical focal-plane position to magnetic rigidity. This rigidity must be converted to excitation energy since we are interested in the excited states of the residual nucleus. From the ion optics of the spectrometer (Equation 3.3) the focal-plane position can be interpreted directly in terms of linear momentum,  $p$ . This interpretation is made possible because the position spectrum is of only tritons which were selected as explained in Section 4.2.1.

To perform the energy calibration, the well-defined peaks of the  $^{24}\text{Mg}(p,t)^{22}\text{Mg}$  calibration runs were used. These peaks correspond to well known excited states in  $^{22}\text{Mg}$  found by performing similar  $^{24}\text{Mg}(p,t)^{22}\text{Mg}$  reactions [44]. The focal-plane positions (labelled (a)-(f) in Figure 4.18) were paired with the corresponding known excitation energy values. Table 4.4 shows the correspondence between the focal-plane positions and excitation energies. The sections below describes the energy calibration process which comprises of 2 steps; position to momentum calibration and momentum to energy conversion.

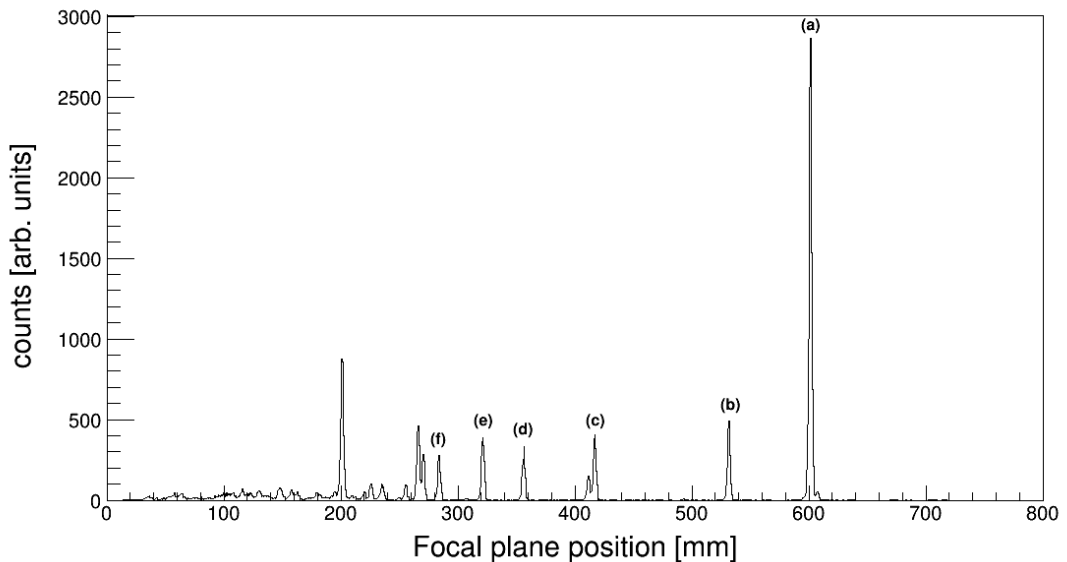


Figure 4.18: The corrected focal-plane position spectrum ( $x_{FP}$ ) for  $^{22}\text{Mg}$ .

Table 4.4: The focal-plane positions with resolution (FWHM), corresponding excitation energies and spin-parities ( $J^\pi$ ) for the dominant states in the focal plane spectrum are listed. These are used to determine the energy calibration.

Label	$x_{FP}$ [mm]	FWHM [mm]	Excitation energy [MeV] [44]	$J^\pi$ [44]
(a)	601.4	2.741	0	$0^+$
(b)	531.7	2.721	1.24702(3)	$2^+$
(c)	417.1	2.811	3.30822(6)	$4^+$
(d)	356.4	2.790	4.402(3)	$2^+$
(e)	321.4	2.892	5.0354(5)	$2^+$
(f)	284.1	2.766	5.7114(7)	$2^+$

#### 4.3.2.1 Position to momentum calibration

The focal-plane position of each state is extracted by fitting with an exponentially tailed Gaussian function and extracting the mean position of the state. Exponentially tailed Gaussian functions are typically used to model processes where some fraction of the ejectile energy is lost [45]. In this case the energy lost is due to target energy losses. The exponentially tailed Gaussian function is given by [45]:

$$G(x; \mu, \sigma, \kappa) = \begin{cases} Ae^{-\frac{(x-\mu)^2}{2\sigma^2}}, & \kappa \geq \frac{x-\mu}{\sigma} \\ Ae^{\frac{\kappa^2}{2} - (\kappa(x-\mu)/\sigma)}, & \kappa < \frac{x-\mu}{\sigma} \end{cases} \quad (4.7)$$

where  $A$  is the amplitude of the functions,  $\mu$  is centroid energy,  $\sigma$  the resolution for the contaminant state and  $\kappa$  is the matching parameter giving the number of standard deviations from the centroid where the function switches from the Gaussian form to the exponential form.

Following the pairing of the focal plane position and the excited states in  $^{22}\text{Mg}$ , the focal plane triton energies of the identified states were then calculated using a relativistic kinematics code and were subsequently converted to rigidity ( $B\rho$ ) values. This is the position to rigidity calibration. The calculated  $B\rho$  values of the identified states are shown in Table 4.5. To complete the rigidity calibration, the focal plane positions were then plotted against calculated rigidity values, as shown in Figure 4.19 and were fitted with a second order polynomial given by:

$$B\rho = g(x; d, e, f) = dx_{FP}^2 + ex_{FP} + f. \quad (4.8)$$

The resulting calibration parameters, ( $d$ ,  $e$  and  $f$ ) are listed in Table 4.6. To complete the position to momentum calibration step, the value for momentum is obtained by multiplying the  $B\rho$  in Equation 4.8 by the charge of the tritons ( $+1$ ) as Equation 3.2 suggests.

Table 4.5: Table showing the focal-plane position and corresponding  $B\rho$  values for the  $^{24}\text{Mg}(p,t)^{22}\text{Mg}$  reaction.

Label	$x_{FP}$ [mm]	$B\rho$ [T mm]	Excitation energy [MeV] [44]
(a)	601.403	2217.96	0
(b)	531.734	2200.63	1.24702(3)
(c)	417.079	2171.68	3.30822(6)
(d)	356.345	2156.15	4.402(3)
(e)	321.422	2147.11	5.0354(5)
(f)	284.048	2137.41	5.7114(7)

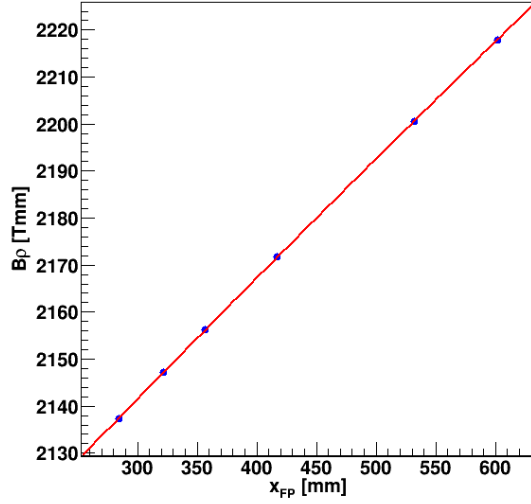


Figure 4.19: The rigidity calibration.

Table 4.6: Focal-plane position to momentum calibration parameters

Parameter	Value	Uncertainty	Units
d	$-2.09 \times 10^{-5}$	$5.7 \times 10^{-7}$	T/mm
e	0.2723	0.00051	T
f	2061.7	0.11	T mm

#### 4.3.2.2 Momentum to energy conversion

The excitation energy,  $E_x$  derived from two-body kinematics [46] is given by:

$$E_x = E_1 + m_2 + \sqrt{p_3^2 - m_3^2} - (p_1^2 + p_3^2 - 2p_1p_3 \cos \theta + m_4^2)^{\frac{1}{2}} \quad (4.9)$$

where the subscripts 1, 2, 3 and 4 represent the projectile, target, ejectile and recoil nuclei, respectively. The value for  $p_3$  (the ejectile momentum) is obtained from the  $B\rho$  calculation

as mentioned in the section above.

The targets used in this experiment are thick and tritons travelling through it will inevitably lose energy. This energy does not reach the focal plane detector system. This makes the calculation of the excitation energy to be sensitive to the target thickness. Corrections to account for this energy loss were made according to the energy losses from SRIM [47], see Appendix A for detailed description of the energy losses. The incorporation of the energy loss into the kinematics calculations is detailed in Appendix B of Ref. [39].

### 4.3.2.3 The excitation energy spectra of $^{22}\text{Mg}$

The calibrated  $^{22}\text{Mg}$  excitation-energy spectrum can be seen in Figure 4.20. The identified states used in the calibration are labelled (a)-(f). All the identified peaks were fitted with an exponentially tailed Gaussian distribution and the position of the peak was then determined by the mean of the Gaussian part.

A comparison of the energy values for the excited states of  $^{22}\text{Mg}$  obtained in this work and those given in the Evaluated Nuclear Structure Data File (ENSDF) [44] can be found in Table 4.7. These comparisons were made for the verification of the peak identification and rough calibration. The final uncertainties in all identified levels are quoted as statistical and systematic separately. The statistical uncertainty (calibration uncertainty) is taken from the fit. Systematic uncertainties include that of the target thickness ( $\pm 0.07 \text{ mg/cm}^2$ ), target energy loss, and the reaction Q-value of  $^{24}\text{Mg}(p,t)^{22}\text{Mg}$  (0.3-keV [26]), or in other words the uncertainty in the masses of the nuclei involved. Table 4.8 shows the systematic uncertainty budget.

Table 4.7: A comparison of the energy values for the excited states of  $^{22}\text{Mg}$  obtained in this experiment and those from the ENSDF. Systematic of 4 keV in the current experiment.

$J^\pi$ [44]	Excitation energy [keV] [44]	This work [keV]	Residual [keV]
$0^+$	g.s.	g.s.	-
$2^+$	1247.02(3)	1247.6(0.6)(4)	0.6
	3308.22(6)	3308.5(0.85)(4)	0.54
$(2)^+$	4402(3)	4404.4(0.6)(4)	2.43
$(2)^+$	5035.4(5)	5035.3(0.7)(4)	0.32
$2^+$	5711.4(7)	5710.8(0.7)(4)	-0.16
$0^+$	5953.8(8)	5955.4(0.6)(4)	1.93
$0^+$	6036.2(8)	6036.6(0.8)(4)	2.99

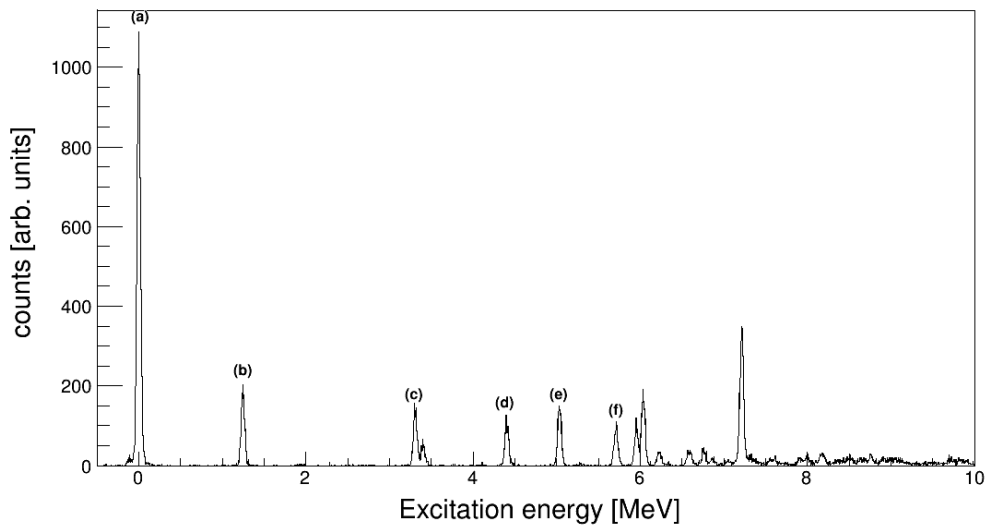


Figure 4.20: The calibrated excitation energy of  $^{22}\text{Mg}$ . The states labelled (a)-(f) corresponds to the same states from the  $x_{FP}$  spectrum used in the calibration (see Figure 4.18 and Table 4.4).

Table 4.8: Systematic uncertainty budget for this data analysis. For the origin of each contribution of the uncertainty, see the text. The total combined systematic uncertainty is the sum in quadrature of the individual components.

Origin	Magnitude	Contribution [keV]
Target thickness	10%	2
Energy loss	0.01%	3
Mass	From Ref. [26]	0.3
Total		4

#### 4.4 The excitation energy spectra of $^{48}\text{Cr}$

Figure 4.21 shows the generated excitation energy spectra of  $^{48}\text{Cr}$ . The spectra has two important features: the first being the observed states in the region of astrophysical importance (9 - 14 MeV in excitation energy). These states in  $^{48}\text{Cr}$  along with others are discussed in detail in Chapter 5 of this dissertation. The second main feature of the spectra emanates from the contaminants associated with the  $^{50}\text{Cr}$  target used in the experiment. These contaminant states appear due to (p,t) reactions on the  $^{12}\text{C}$  and  $^{16}\text{O}$  contaminants present in the  $^{50}\text{Cr}$  target. Section 4.4.1 below detail how these contaminant states were identified in the  $^{48}\text{Cr}$  spectra.

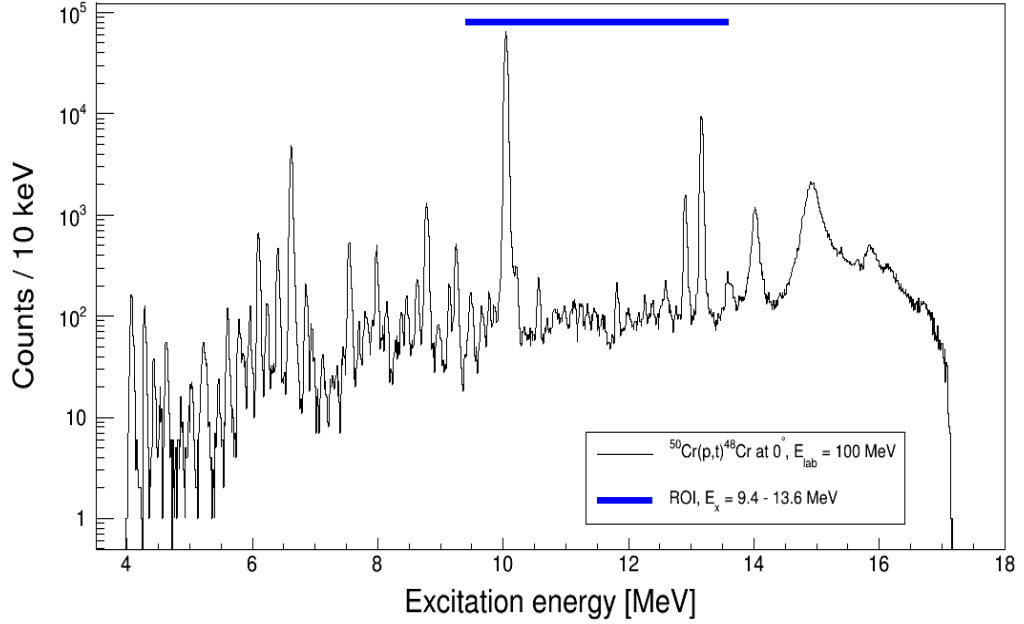


Figure 4.21: The excitation energy spectra of  $^{48}\text{Cr}$ . The blue bar represents the region of astrophysical interest (ROI).

#### 4.4.1 Contaminant states

The impurities of  $^{12}\text{C}$  and  $^{16}\text{O}$  have larger (p,t) cross sections and similar reaction Q-values (see Table 4.9). This makes the natural parity states of  $^{10}\text{C}$  and  $^{14}\text{O}$  a dominant feature in the experimental spectra. The magnetic field settings of the spectrometer also places most of these states in the region of astrophysical interest, making the background identification indispensable. To illustrate this, Figure 4.22 shows the magnetic rigidity of tritons coming from selected ground, and excited states in the different recoil nuclei present in the target. The momentum acceptance of the focal-plane in terms of magnetic rigidity is given for the K600 magnetic field settings used in the experiment (horizontal black line). The field settings were chosen such that the region of interest (labeled as ROI in Figure 4.22) in  $^{48}\text{Cr}$  fall within the middle of the focal plane which was previously calibrated by the low-lying states in  $^{22}\text{Mg}$  (see Section 4.3). To identify the possible background peaks from reactions involving  $^{12}\text{C}$  and  $^{16}\text{O}$ , (p,t) data was taken at  $0^\circ$  with a thin Mylar ( $\text{C}_{10}\text{H}_8\text{O}_4$ ) target.

Table 4.9: Q-values of different reactions on targets used in the experiment.

Target	Reaction	Q-value (MeV)
$^{50}\text{Cr}$	$^{50}\text{Cr}(\text{p,t})^{48}\text{Cr}$	-15.101(7) [26]
Mylar ( $^{12}\text{C}$ and $^{16}\text{O}$ )	$^{12}\text{C}(\text{p,t})^{10}\text{C}$	-23.35951(0.07) [26]
	$^{16}\text{O}(\text{p,t})^{14}\text{O}$	-20.40562(0.03) [26]

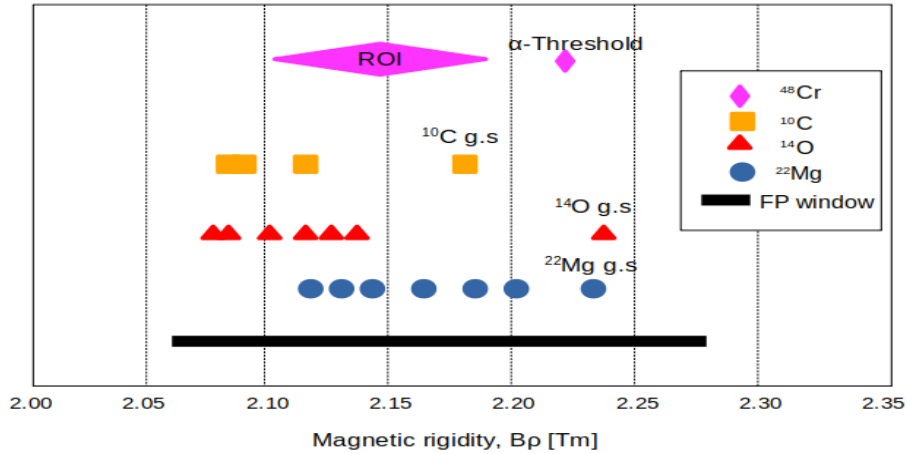


Figure 4.22: Magnetic rigidities ( $B\rho$ ) of tritons coming from selected ground, and excited, states in different recoil nuclei. The black bar represent the momentum coverage of the focal plane for the magnetic field settings of the K600. The regions labeled ROI represents the regions of astrophysical interest in  $^{48}\text{Cr}$ .

#### 4.4.1.1 Carbon contaminants

The location of the  $^{10}\text{C}$  contaminating  $0^+$  ground-state, 3353.7(6)-keV  $2^+$  and the doublet 5220(40)-keV  $2^+$  and 5380(70)-keV  $2^+$  states listed in ENSDF [48] were identified (shown as dashed vertical blue lines in Figure 4.23). Figure 4.23 shows the Mylar (p,t) spectra (red) superimposed on the  $^{50}\text{Cr}$  (p,t) spectra (black) using  $^{12}\text{C}(p,t)^{10}\text{C}$  reaction kinematics.

#### 4.4.1.2 Oxygen contaminants

Using the same procedure outlined for the carbon contaminants but this time with  $^{16}\text{O}(p,t)^{14}\text{O}$  reaction kinematics, the location of the  $^{14}\text{O}$  contaminating ground state  $0^+$ , 5920(10)-keV  $0^+$ , 6272(10)-keV  $3^-$ , 6590(10)-keV  $2^+$ , 7768(10)-keV  $2^+$  and the doublet 9715(20)-keV  $(2)^+$  and 9915(20)-keV  $4^+$  states listed in ENSDF [49] were identified (shown as dashed vertical blue lines in Figure 4.24).

#### 4.4.1.3 Background

The Mylar spectra in Figures 4.23 and 4.24 was scaled to match the oxygen ground state peak. With this normalization the other oxygen peaks match their Cr spectra contaminants counterparts. Interestingly, the background does not scale as much which suggests that the apparent background may be due to the natural broadening of the states at higher excitation energies.

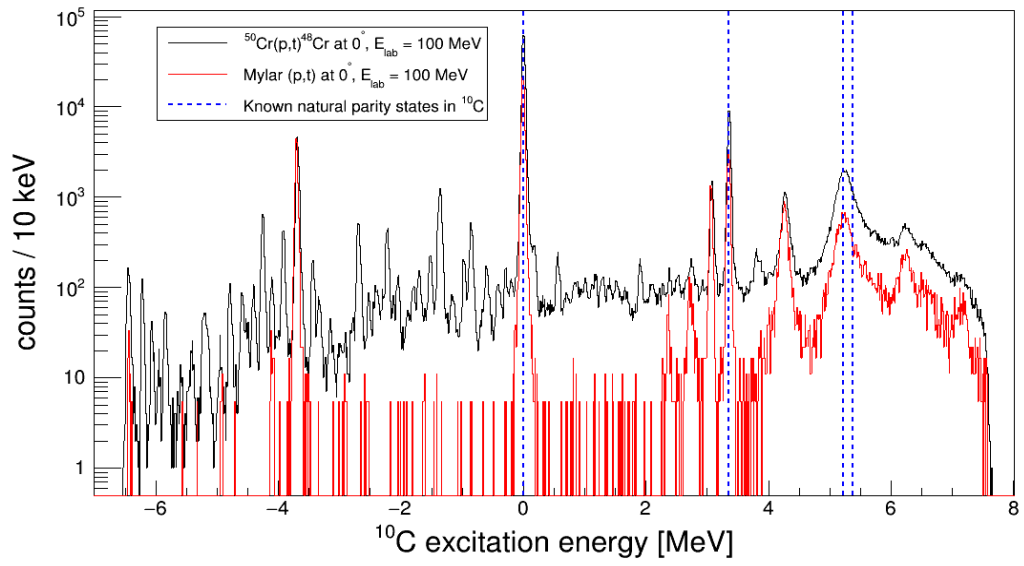


Figure 4.23: Mylar(p,t) spectra (red) superimposed on the  $^{50}\text{Cr}(p,t)$  spectra (black) using  $^{12}\text{C}(p,t)^{10}\text{C}$  reaction kinematics. Dashed vertical blue lines show the location of known  $^{10}\text{C}$  excited states.

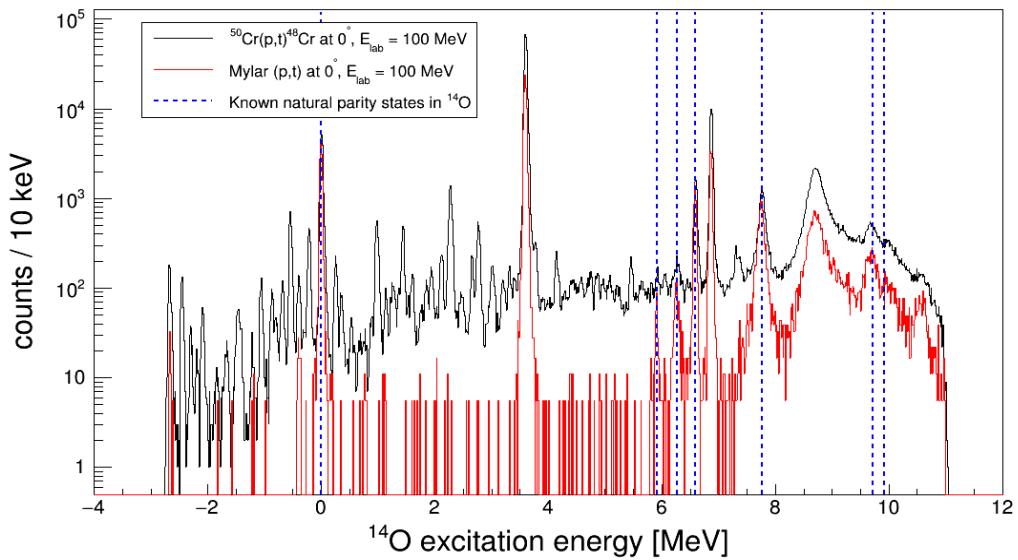


Figure 4.24: Mylar(p,t) spectra (red) superimposed on the  $^{50}\text{Cr}(p,t)$  spectra (black) using  $^{16}\text{O}(p,t)^{14}\text{O}$  reaction kinematics. Dashed vertical blue lines show the location of known  $^{14}\text{O}$  excited states.

#### 4.4.2 Low-lying states in $^{48}\text{Cr}$

Previous  $^{50}\text{Cr}(p,t)^{48}\text{Cr}$  measurements [50–52] have observed states of up to 7.5 MeV. For this work, these states fall outside the calibration region as described in Section 4.4.1. In this section, these states are used to evaluate the calibration. To check the calibration, a residual energy plot between the evaluated low-lying natural parity states in  $^{48}\text{Cr}$  [53] and those observed in this work was plotted (see Figure 4.25 and Table 4.10). The goodness of fit (Figure 4.25) is  $\chi^2_\nu = 0.672$ , indicating a good agreement.

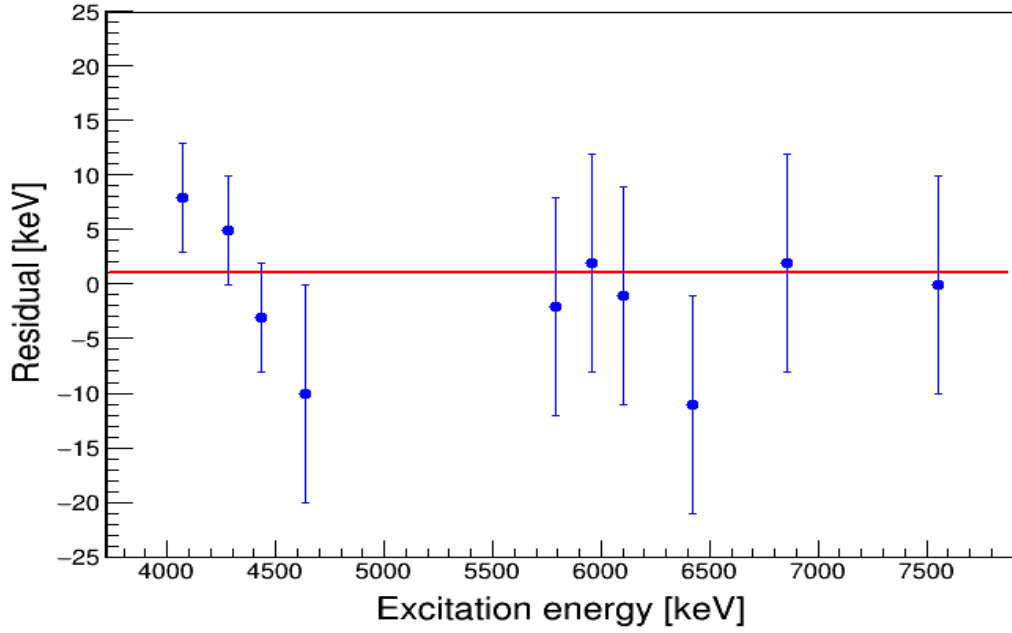


Figure 4.25: Residual energy plot from using low lying states in  $^{48}\text{Cr}$ . The goodness of fit is  $\chi^2_\nu = 0.672$ . Error bars taken from ENSDF [53].

Table 4.10: Energy values of the low-lying excited states of  $^{48}\text{Cr}$  obtained in this experiment and those provided by the ENSDF.

This work [keV]	Excitation energy [keV] [53]	$J^\pi$ [53]
4075(1)(10)	4067(5)	
4285(1)(10)	4280(5)	(0) <sup>+</sup>
4429(2)(10)	4432(5)	(4) <sup>+</sup>
4630(2)(10)	4640(10)	2 <sup>+</sup>
5788(1)(10)	5790(10)	4 <sup>+</sup>
5962(1)(10)	5960(10)	(0) <sup>+</sup>
6099.3(0.5)(10)	6100(10)	2 <sup>+</sup>
6409(1)(10)	6420(10)	(5)
6857(1)(10)	6855(10)	0 <sup>+</sup>
7550(1)(10)	7550(10)	

The final uncertainties in all identified levels are quoted as statistical and systematic separately. The statistical uncertainty (calibration uncertainty) is taken from the Gaussian fit of the observed states. Systematic uncertainties include that of the target thickness ( $\pm 0.115$  mg/cm<sup>2</sup>), target energy loss, and the reaction Q-value of  $^{50}\text{Cr}(p,t)^{48}\text{Cr}$  (7 keV [26]). Table 4.11 shows the systematic uncertainty budget.

Table 4.11: Systematic uncertainty budget for this data analysis. For the origin of each contribution of the uncertainty, see the text. The total combined uncertainty is the sum in quadrature of the individual components.

Origin	Magnitude	Contribution [keV]
Target thickness	10%	5
Energy loss	0.01 %	6
Mass	From Ref. [26]	7
Total		10

# Chapter 5

## Results and Discussion

### 5.1 Level structure of $^{48}\text{Cr}$

In total, 55 states were identified in  $^{48}\text{Cr}$  from this work. Twenty-one (21) states were observed below the  $\alpha$ -threshold (7698(7)-keV [26]) and 34 states above the  $\alpha$ -threshold up to 14 MeV in excitation energy. Of the 34 states above the  $\alpha$ -threshold, 24 lie in the region of astrophysical interest. Forty-five of the 55 observed states were observed for the first time. In this section the observed excited states in  $^{48}\text{Cr}$  are presented along with states published in previous works for comparison. All the identified peaks in the focal plane spectra were fitted with symmetric Gaussian peaks using binned likelihood statistics owing to the low statistics and the position of the peak was then determined by the centroid. The average energy resolution (FWHM) for the states below the  $\alpha$ -threshold is 80 keV, while for states above it is 115 keV. The quoted uncertainties are discussed in section 4.4.2.

#### 5.1.1 States below the $\alpha$ -threshold

To date there have been three experiments performing the (p,t) reaction on  $^{50}\text{Cr}$  to study the level structure of the  $^{48}\text{Cr}$  nucleus [50–52]. All of these past experiments were conducted in the early 1970s, with beam energies ranging from 27-51 MeV, focusing on states below the  $\alpha$ -threshold. Table 5.1 shows a compilation of the natural parity states observed in these previous studies including from  $^{46}\text{Ti}(^3\text{He},n)^{48}\text{Cr}$  measurements [54, 55] and those from this work. Figure 5.1 shows the excitation energy spectrum for states below the  $\alpha$ -threshold. In this figure, the locations of the evaluated states are superimposed into the spectra. Solid blue lines show states previously observed in (p,t) measurements [51]. Red dotted-dashed lines show states previously observed in ( $^3\text{He},n$ ) measurements [54, 55]. The purple dashed lines shows a state previously observed in  $^{48}\text{Mn}$   $\beta^+$  decay measurements [56].

Table 5.1: List of states in  $^{48}\text{Cr}$  below the  $\alpha$ -threshold.

This work	Shepard <i>et al.</i> [52]	Dorenbusch <i>et al.</i> [51]	Bruandet <i>et al.</i> [50]	Alford <i>et al.</i> [54]	Evers <i>et al.</i> [55]					
$^{50}\text{Cr}(p,t)^{48}\text{Cr}$	$^{50}\text{Cr}(p,t)^{48}\text{Cr}$	$^{50}\text{Cr}(p,t)^{48}\text{Cr}$	$^{50}\text{Cr}(p,t)^{48}\text{Cr}$	$^{46}\text{Ti}(^3\text{He},n)^{48}\text{Cr}$	$^{46}\text{Ti}(^3\text{He},n)^{48}\text{Cr}$					
$E_x$ [keV]	$E_x$ [keV]	$J^\pi$	$E_x$ [keV]	$J^\pi$	$E_x$ [keV]	$J^\pi$	$E_x$ [keV]	$J^\pi$	$E_x$ [keV]	$J^\pi$
4075(1)(10)	4050(20)	2 <sup>+</sup>	4067(5)	3 <sup>-</sup>	-	-	-	-	-	-
-	-	-	-	-	4140(30)	4 <sup>+</sup>	-	-	-	-
4285(1)(10)	4240(20)	0 <sup>+</sup>	4280(5)	0 <sup>+</sup>	-	-	-	-	-	-
-	-	-	-	-	4360(30)	0 <sup>+</sup>	-	-	-	-
4429(2)(10)	-	-	4432(5)	4 <sup>+</sup>	-	-	-	-	-	-
-	-	-	-	-	4520(30)	4 <sup>+</sup>	-	-	-	-
4530(4)(10)	-	-	-	-	-	-	-	-	-	-
4630(2)(10)	-	-	4640(10)	2 <sup>+</sup>	-	-	-	-	-	-
4858(4)(10)	-	-	-	-	-	-	-	-	-	-
5020(3)(10)	-	-	-	-	-	-	-	-	-	-
5228(2)(10)	-	-	-	-	-	-	-	-	-	-
5468(4)(10)	-	-	-	-	-	-	5480(50)	0 <sup>+</sup>	5430(30)	0 <sup>+</sup>
5609(1)(10)	-	-	-	-	-	-	-	-	-	-
-	5670(20)	0 <sup>+</sup>	-	-	-	-	-	-	-	-
5788(1)(10)	-	-	5790(10)	4 <sup>+</sup>	-	-	-	-	-	-
-	-	-	-	-	5880(30)	4 <sup>+</sup>	-	-	-	-
5962(1)(10)	-	-	5960(10)	0 <sup>+</sup>	-	-	-	-	6010(30)	-
6099(0.5)(10)	-	-	6100(10)	2 <sup>+</sup>	-	-	-	-	-	-
-	-	-	-	-	6180(30)	2 <sup>+</sup>	-	-	-	-
6236(1)(10)	-	-	-	-	-	-	-	-	-	-
6409(0.5)(10)	-	-	6420(10)	(5) <sup>-</sup>	-	-	-	-	-	-
6857(1)(10)	-	-	6855(10)	0 <sup>+</sup>	-	-	-	-	-	-
6951(2)(10)	-	-	-	-	-	-	-	-	-	-
7127(3)(10)	-	-	-	-	-	-	-	-	-	-
7306(5)(10)	-	-	-	-	-	-	-	-	-	-
7465(5)(10)	-	-	-	-	-	-	-	-	-	-
7550(0.5)(10)	-	-	7550(10)	-	-	-	-	-	-	-

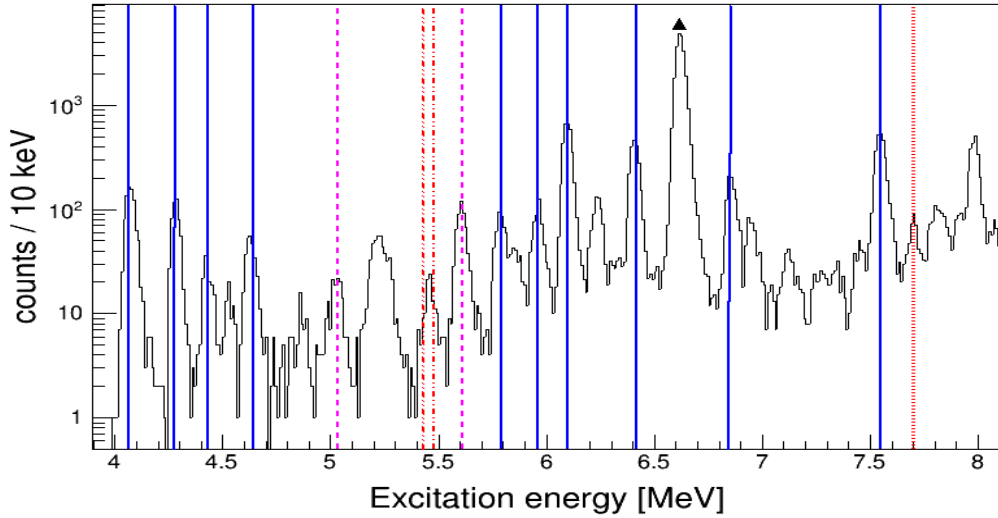


Figure 5.1: Excited states below the  $\alpha$ -threshold in  $^{48}\text{Cr}$ . The fine-dashed red line shows the  $\alpha$ -threshold (7698(7)-keV [26]). Solid blue lines show states observed in (p,t) measurements [51]. Red dotted-dashed lines show states previously observed in ( $^3\text{He}$ ,n) measurements [54, 55]. Purple dashed line shows a state observed in  $^{48}\text{Mn}$   $\beta^+$  decay measurements [56]. The state marked with a black triangles is the  $^{14}\text{O}$  ground state contaminant.

The work of Dorenbusch et al. [51] offers the most comprehensive number of states. Almost all of the states agree well with previous works with the exception of the 4067(5)-keV state that is slightly lower than the value obtained in the present work (4075(1)(10)-keV) but is in agreement within the uncertainties. The state may be a doublet as suggested in the work of Shepard et al. [52].

Only 3 states from the work of Shepard et al. fall within the excitation energy range covered in this work. The 4050(20)-keV and the 4240(20)-keV states agree well with the present work. However, the 5670(20)-keV  $J^\pi = 0^+$  state is an outlier. It is not observed in the present work nor is it observed in the works of Dorenbusch et al. and Braundet et al. It has a  $J^\pi = 0^+$  assignment which should be strongly excited in a  $0^\circ$  measurement such as the one analysed in this dissertation. The state is not discussed in detail in the work of Shepard et al. and its  $0^+$  assignment is based on the “strong enhancement of this state relative to its neighbors at low scattering angles” [52]. This 5670(20) keV state may be the 5609(1)(10)-keV state observed in this work or it may indeed be a different excited state.

None of the states observed in the work of Braundet et al. [50] match the states observed in this work and the works by Shepard et al. and Dorenbusch et al. Judging from the  $J^\pi$  assignments in the Braundet et al. work in comparison with the  $J^\pi$  assignments from Shepard et al. and Dorenbusch et al., the states in the work of Braundet et al. have an apparent +100 keV energy-shift. By shifting all the states in Braundet et al. (see Table 5.1)

by -100 keV, there is a much better agreement between the states observed in Braundet et al. and those observed in this current work and previous. This plausible systematic up-shift in the energy values may be due to the mass uncertainty used to calculate these excitation energies. In the 1985 nuclear data sheets for  $A = 48$ , the energy-shift is quoted as an  $\approx 80$  KeV calibration error [57].

A common theme amongst the previous studies [50–52] are the missing states between 4640(10)-keV and 5790(10)-keV. From the present work, 4 states have been observed within this gap. These states may be weakly populated at higher scattering angles. The only evidence of natural-parity states within this gap comes from a strongly excited  $J^\pi = 0^+$  state observed in  $^{46}\text{Ti}(^3\text{He},n)^{48}\text{Cr}$  measurements [54,55] and  $^{48}\text{Mn}$   $\beta^+$  decay measurements [56].

### 5.1.2 States above the $\alpha$ -threshold

Few levels are known in  $^{48}\text{Cr}$  above the  $\alpha$ -threshold. The known states are observed in  $(^3\text{He},n)$  measurements by Alford et al. [54] and Evers et al. [55] looking for  $J^\pi = 0^+$  states in the fp-shell. Figure 5.2 shows the excitation energy spectrum of  $^{48}\text{Cr}$  above the  $\alpha$ -threshold. Due to the low statistics and the increase in the natural width of the states at higher excitation energies, we increased the binning from about 10 keV for states below the  $\alpha$ -threshold to about 22 keV for states above the  $\alpha$ -threshold. Table 5.2 shows a compilation of the natural parity states observed in  $^{46}\text{Ti}(^3\text{He},n)^{48}\text{Cr}$  measurements [54,55] and this work. A good agreement between this work and the  $(^3\text{He},n)$  measurements [54,55] is observed.

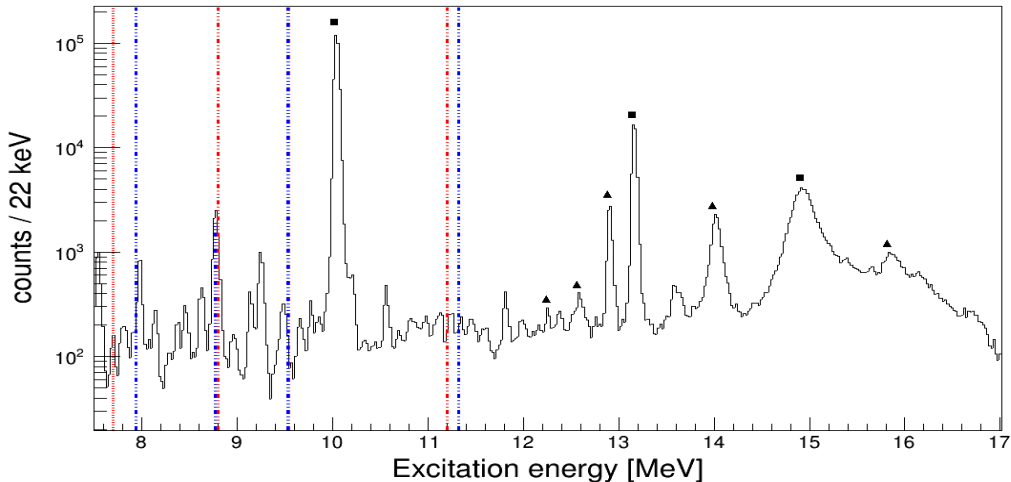


Figure 5.2: Excited states above the  $\alpha$ -threshold in  $^{48}\text{Cr}$ . The fine-dashed red line shows the  $\alpha$ -threshold (7.698(7)-MeV). Blue dotted-dashed lines show states observed in  $(^3\text{He},n)$  measurements by Evers et al. [55]. Red dotted-dashed lines show states observed in  $(^3\text{He},n)$  measurements by Alford et al. [54] (see Table 5.2). States marked with black triangles are  $^{14}\text{O}$  contaminants, states marked with black squares are  $^{10}\text{C}$  contaminants.

Table 5.2: List of states in  $^{48}\text{Cr}$  above the  $\alpha$ -threshold.

This work	Alford <i>et al.</i> [54]	Evers <i>et al.</i> [55]		
$^{50}\text{Cr}(p,t)^{48}\text{Cr}$	$^{46}\text{Ti}(^3\text{He},n)^{48}\text{Cr}$	$^{46}\text{Ti}(^3\text{He},n)^{48}\text{Cr}$		
$E_x$ [keV]	$E_x$ [keV]	$J^\pi$	$E_x$ [keV]	$J^\pi$
7700(2)(10)	-	-	-	-
7817(2)(10)	-	-	-	-
7982(1)(10)	-	-	7940(30)	0 <sup>+</sup>
8142(1)(10)	-	-	-	-
8379(2)(10)	-	-	-	-
8465(1)(10)	-	-	-	-
8630(1)(10)	-	-	-	-
8779(0.3)(10)	8800(50)	0 <sup>+</sup>	8770(30)	0 <sup>+</sup>
8969(3)(10)	-	-	-	-
9145(1)(10)	-	-	-	-
9253(1)(10)	-	-	-	-
9487(1)(10)	9540(50)	0 <sup>+</sup>	9530(30)	0 <sup>+</sup>
9668(2)(10)	-	-	-	-
9777(1)(10)	-	-	-	-
9863(3)(10)	-	-	-	-
10198(3)(10)	-	-	-	-
10332(6)(10)	-	-	-	-
10565(1)(10)	-	-	-	-
10697(5)(10)	-	-	-	-
10837(5)(10)	-	-	-	-
10970(4)(10)	-	-	-	-
11133(3)(10)	11200(100)	0 <sup>+</sup>	-	-
11243(2)(10)	-	-	-	-
11346(4)(10)	-	-	11320(30)	0 <sup>+</sup>
11454(4)(10)	-	-	-	-
11594(4)(10)	-	-	-	-
11816(1)(10)	-	-	-	-
11994(4)(10)	-	-	-	-
12170(4)(10)	-	-	-	-
12262(3)(10)	-	-	-	-
12384(3)(10)	-	-	-	-
12586(3)(10)	-	-	-	-
12777(5)(10)	-	-	-	-
13609(2)(10)	-	-	-	-

This end of the spectrum (above the  $\alpha$ -threshold) has most of the contaminant states with the exception of the  $^{14}\text{O}$  ground-state which is located below the  $\alpha$ -threshold. The most prominent contaminant peak is the  $^{10}\text{C}$  ground state sitting just over  $E_x, ^{48}\text{Cr} = 10$  MeV, with a FWHM of 57 keV. The state is well within the excitation energy range of interest. Its broad footprint will conceal some  $^{48}\text{Cr}$  states. For example, one of these states can be seen on the shoulder of this state at about  $E_x, ^{48}\text{Cr} = 10.2$  MeV. Since this is a zero-degree measurement, kinematic shifts between the Cr states and the contaminant states are very small, making it easy for prominent contaminant states to conceal states of interest. The same applies to the 3.353-MeV  $^{10}\text{C}$  state sitting just over  $E_x, ^{48}\text{Cr} = 13$  MeV and the 6.590-MeV  $^{14}\text{O}$  state sitting below  $E_x, ^{48}\text{Cr} = 13$  MeV. Looking at the normalised spectra in Figures 4.23 and 4.24 which were normalised such that the ground-state of  $^{14}\text{O}$  matches the experimental data, most of the other  $^{14}\text{O}$  states also scale to fit the experimental data. The two  $^{14}\text{O}$  states; the 5.920- and 6.272-MeV sitting at  $E_x, ^{48}\text{Cr} = 12.2$ - and  $E_x, ^{48}\text{Cr} = 12.6$ -MeV respectively, do not explain all of the experimental strength to match the experimental data as the other  $^{14}\text{O}$  states. It implies that, unlike the other states which are completely dominated by a contaminant, this excitation region comes from potential  $^{48}\text{Cr}$  states.

## 5.2 Nuclear-level cumulatives

In this section the observed and microscopic nuclear-level cumulatives of  $^{48}\text{Cr}$  are presented. The experimental nuclear-level cumulatives are extracted by the direct counting of the observed states from this work and previous works. For a more complete comparison, the experimental nuclear cumulatives from this work were supplemented with the 7 known natural-parity states in  $^{48}\text{Cr}$  from 0 to 4 MeV obtained in previous (p,t) measurements [50–52] (see Tables 5.3, 5.1 and 5.2 as well as black cumulative staircase in Figure 5.3). The comparison of the results is conducted under the assumptions that all the observed states are natural-parity states. The validity of these assumptions emanate from the tendency of (p,t) reactions favouring natural-parity states (see Section 1.4).

Table 5.3: Energy values of the first 7 excited states of  $^{48}\text{Cr}$  provided by the ENSDF [53].

Excitation energy [keV] [53]	$J^\pi$ [53]
0	$0^+$
750(5)	$2^+$
1845(5)	$(4)^+$
3420(20)	$(0)^+$
3452(5)	6, (5)
3527(5)	
3630(5)	(2,3)

To compare with the experimental results, we made use of the microscopic Hartree-Fock-Bogolyubov (HFB) level densities with Hilaire’s combinatorial tables [32]. These level densities are available in the online Reference Input Parameter Library (RIPL-3) [33]. From these table we selected only natural parity states ranging from  $J^\pi = 0^+$  to  $J^\pi = 49^-$  to compute the nuclear level cumulatives (see red cumulative staircase in Figure 5.3). This is in accordance with the original assumption that only natural parity states are involved in the  $^{44}\text{Ti}(\alpha, p)^{47}\text{V}$  reaction (see Section 1.4). These (p,t) measurements, conducted at high energies and at a scattering angle of  $0^\circ$ , highly favour low-spin states and therefore, to include a spin-cut off, we selected only natural parity states:  $J^\pi = 0^+, 1^-, 2^+, 3^-$  and  $4^+$  (see green cumulative staircase in Figure 5.3).

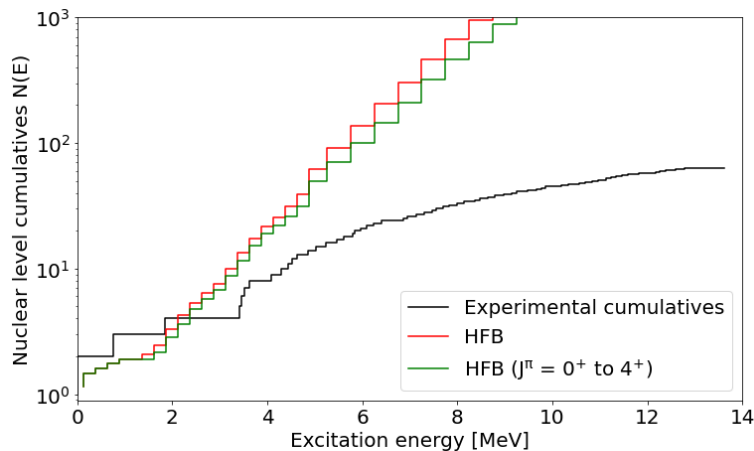


Figure 5.3: Nuclear level cumulatives in  $^{48}\text{Cr}$ . The black staircase are the experimental nuclear level cumulatives obtained from this work and previous work (see text for details). The red staircase nuclear level cumulatives are the microscopic Hartree-Fock-Bogolyubov (HFB) (Skyrme force) with Hilaire’s combinatorial tables for  $J = 0 - 49$  extracted from RIPL [32]. The green staircase nuclear level cumulatives are the microscopic Hartree-Fock-Bogolyubov (HFB) (Skyrme force) with Hilaire’s combinatorial tables for  $J^\pi = 0^+, 1^-, 2^+, 3^-$  and  $4^+$  extracted from RIPL.

The observed experimental nuclear cumulatives in Figure 5.3 are low as compared to the HFB predicted cumulatives. The microscopic model predict a steep increase in the level cumulatives starting at about 2 MeV. This is in contrast with the experimental cumulatives which gently increase and begin to saturate at higher excitation energies. In the Hauser-Feshbach formalism (see Section 2.2.1), the number of levels are expected to be high at higher excitation energies. The observed cumulatives level-off at excitation energies greater than 9 MeV. This leveling off hints that the levels are packed closely together suggesting that the experimental resolution is not good enough to resolve states. This may also mean that the states in  $^{48}\text{Cr}$  are not numerous. In the energy region, 0 - 9 MeV, the experimental resolution is better than the separation of states. Fewer levels in this region are observed compared to the HFB model calculations with and without limited spin (red and green

cumulatives in Figure 5.3, respectively). The small number of levels at this low energy range where the resolution is good enough hint that as you go higher up in energy there are fewer levels in  $^{48}\text{Cr}$  than HF predictions. This implies low level density in  $^{48}\text{Cr}$ .

Since the red and green cumulative staircases in Figure 5.3 reveal an overestimation of the levels in  $^{48}\text{Cr}$  by the HFB model, the use of microscopic level densities in the HF formalism may lead to a misestimation of the reaction rate. However, further experimental work is required to obtain the spin and parity assignments of the observed states. With the energies and spins of resonance states identified, a reaction rate calculation can be performed using as input experimental nuclear cumulatives and compared to the HF rate using microscopic models.

## Chapter 6

# Conclusion and Outlook

A  $^{50}\text{Cr}(p,t)^{48}\text{Cr}$  reaction was measured by the K600 magnetic spectrometer with an intention to excite natural parity state in  $^{48}\text{Cr}$  that could act as resonances for the  $^{44}\text{Ti}(\alpha,p)^{47}\text{V}$  reaction that controls the destruction of  $^{44}\text{Ti}$  in core-collapse supernovae. By analysing data from a  $^{50}\text{Cr}(p,t)^{48}\text{Cr}$ , this dissertation has reported 55 excited states observed in  $^{48}\text{Cr}$ . Forty-five (45) of 55 states are observed for the first time in this work. Most important of these states are the 24 states observed in the region of astrophysical interest. These are the states that could act as resonances for the  $^{44}\text{Ti}(\alpha,p)^{47}\text{V}$  reaction.

From this spectroscopic data, nuclear level cumulatives were extracted and compared with microscopic level cumulatives. The result shows an overestimation of the cumulatives by the microscopic HFB level density model. Nuclear level cumulatives and hence, nuclear level densities being one of the most important inputs in the HF model, this result implies that when microscopic levels may lead to a misestimation of the cross sections and reaction rates.

However, to better understand the implications of these results, it will be good in future studies to obtain the spin and parity assignments of the observed states. This can be achieved by looking at charged particle decays from the excited states in  $^{48}\text{Cr}$ . In addition to this, charged-particle decays from  $^{48}\text{Cr}$  may reveal hidden  $^{48}\text{Cr}$  states that were unresolved or obscured by contaminants. With the energies and spins of resonance states identified from the (p,t) reaction along with shell model calculations or mirror nucleus information for resonance strengths, an indirect  $^{44}\text{Ti}(\alpha,p)^{47}\text{V}$  reaction rate can be calculated and thus, offering a direct comparison of the reaction rate calculated using the Hauser-Feshbach model.

# Appendix A

## Target energy loss calculations

Following the lineshape corrections, the states in the position spectra were observed to be having some high energy tail. Amongst other things, the high energy tail in the spectrum gives a hint that there are energy losses experienced by the tritons. A bulk of the losses occur in the target. A correction for the energy loss of tritons in the target has to be taken into account in the calibration procedure. Target energy losses are governed by Bethe-Bloch equation is given by [27]:

$$-\frac{dE}{dx} \approx \frac{4\pi e^4 Z_p^2}{m_e v^2} \left( N_A \rho \frac{Z_t}{M_t} \right) \ln \left( \frac{2m_e v^2}{I} \right) \quad (\text{A.1})$$

where  $e$  is the electric charge,  $m_e$  is the rest mass of an electron,  $v$  is the velocity of the ionising projectile,  $Z_p$  and  $Z_t$  is the proton number of the projectile and target, respectively,  $M_t$  is the atomic mass of the target,  $N_A$  is Avogadro's number,  $\rho$  is the density of the target material and lastly,  $I$  is an average excitation and ionization potential of the target material.

To model for the energy losses, the Stopping and Range of Ions in Matter software known as SRIM was used [47]. In SRIM, a projected range was obtained and plotted against particles energy. The projected range is the distance travelled by an ion before coming to rest and is given by [27]:

$$R = \int_0^{E_0} \left( \frac{dE}{dx} \right)^{-1} dE \quad (\text{A.2})$$

This projected range was then converted in terms of areal density in accordance to the specification of the targets by multiplying with the density of the target. The projected range-energy model given by:

$$h(E; i, j, k) = iE^2 + jE + k \quad (\text{A.3})$$

The energy loss models are shown in Figure A.2 and the parameters of the models in Table A.1.

The assumption is that on average the  $^{24}\text{Mg}(p,t)^{22}\text{Mg}$  reaction takes place at the center of the  $^{24}\text{Mg}$  target and the  $^{50}\text{Cr}(p,t)^{48}\text{Cr}$  reaction take place at the center of the  $^{50}\text{Cr}$  part of the carbon backed  $^{50}\text{Cr}$  target. Following this assumption, the triton energy loss is calculated for half of the target thickness in the case of the  $^{24}\text{Mg}$  target and in the case of the  $^{50}\text{Cr}$  target, the tritons lose more energy as it travels through the  $^{12}\text{C}$  thickness. Figure A.1 shows the geometry of the  $^{50}\text{Cr}$  carbon-backed target.

By solving for energy in the model, the energy losses experienced by the beam and the ejectiles were accounted for and implemented included in relativistic kinematics code calculations of the excitation energies.

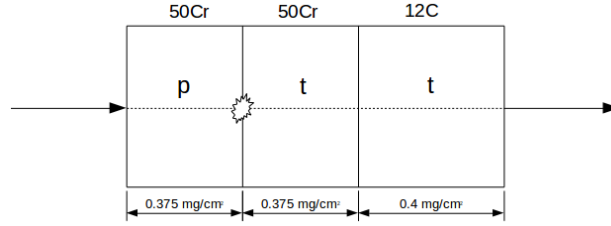


Figure A.1: Target geometry of the  $^{50}\text{Cr}$  target used in this experiment. The beam is from left to right. p = protons and t = tritons.

Table A.1: Table showing the parameters of the energy loss models.

Model	Parameter	Value	Error $\pm$	Units
protons in $^{24}\text{Mg}$	i	0.625	0.0078	$\text{mg}/\text{cm}^2\text{MeV}^2$
	j	41	1.5	$\text{mg}/\text{cm}^2\text{MeV}$
	k	-975	69.9	$\text{mg}/\text{cm}^2$
tritons in $^{24}\text{Mg}$	i	0.299	0.0022	$\text{mg}/\text{cm}^2\text{MeV}^2$
	j	12.4	0.34	$\text{mg}/\text{cm}^2\text{MeV}$
	k	-195	12.7	$\text{mg}/\text{cm}^2$
protons in $^{50}\text{Cr}$	i	0.702	0.0082	$\text{mg}/\text{cm}^2\text{MeV}^2$
	j	47	1.6	$\text{mg}/\text{cm}^2\text{MeV}$
	k	-1041	73.5	$\text{mg}/\text{cm}^2$
tritons in $^{50}\text{Cr}$	i	0.325	0.0078	$\text{mg}/\text{cm}^2\text{MeV}^2$
	j	17	1.18	$\text{mg}/\text{cm}^2\text{MeV}$
	k	-306	43.58	$\text{mg}/\text{cm}^2$
tritons in $^{12}\text{C}$	i	0.276	0.0053	$\text{mg}/\text{cm}^2\text{MeV}^2$
	j	9.7	0.805	$\text{mg}/\text{cm}^2\text{MeV}$
	k	-155	29.7	$\text{mg}/\text{cm}^2$

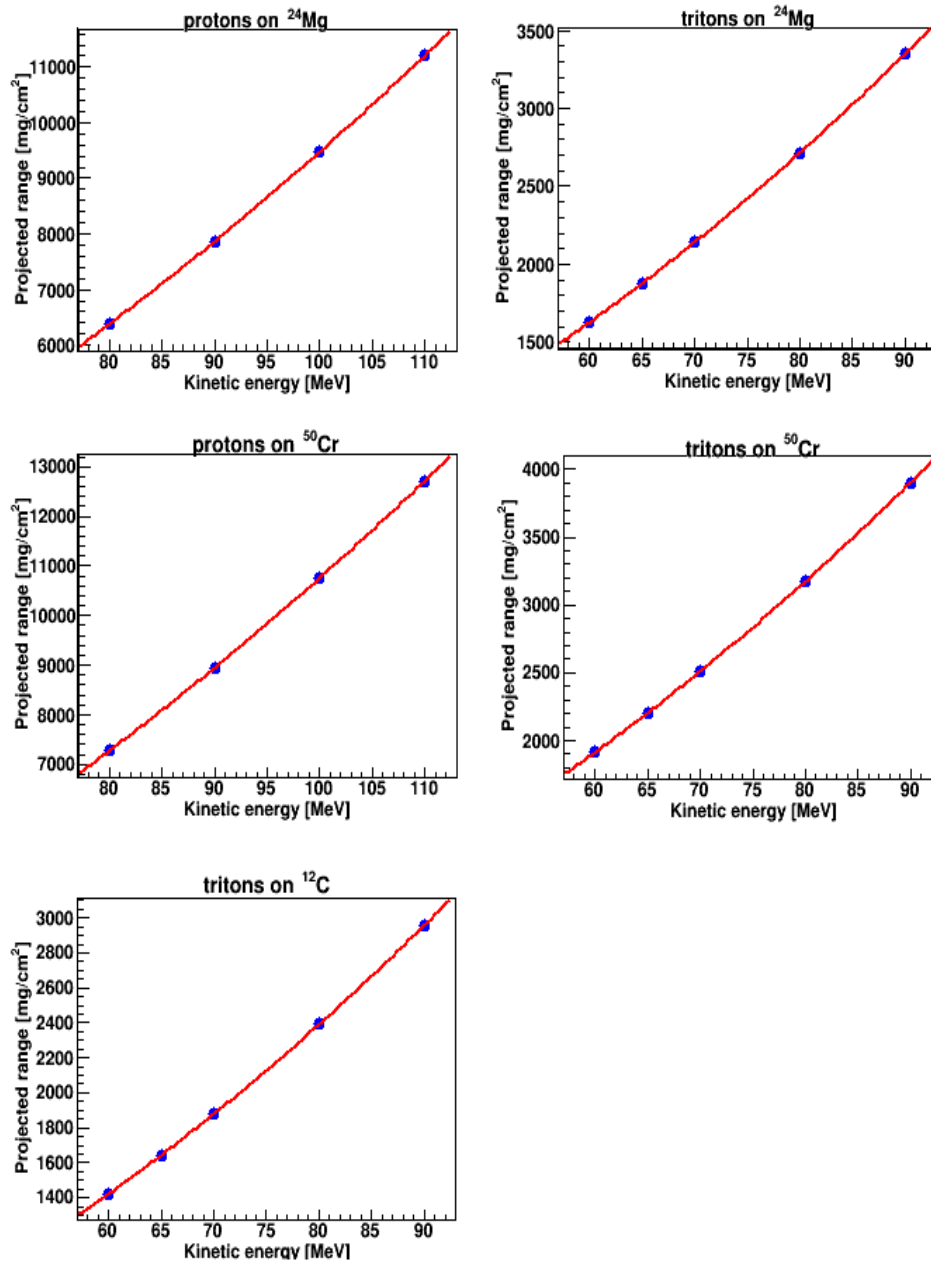


Figure A.2: Graphs of energy and projected range.

# Bibliography

- [1] W. Wang, “Detections of  $^{44}\text{Ti}$  signals in young supernova remnants,” *Proceedings of the 15th International Symposium on Origin of Matter and Evolution of Galaxies (OMEG15)*, 2019.
- [2] S. Woosley and R. D. Hoffman, “ $^{57}\text{Co}$  and  $^{44}\text{Ti}$  production in SN 1987A,” *The Astrophysical Journal*, vol. 368, pp. L31–L34, 1991.
- [3] R. D. Hoffman, S. Sheets, J. Burke, N. Scielzo, T. Rauscher, E. Norman, S. Tumey, T. Brown, P. Grant, A. Hurst, *et al.*, “Reaction rate sensitivity of  $^{44}\text{Ti}$  production in massive stars and implications of a thick target yield measurement of  $^{40}\text{Ca}(\alpha, \gamma)^{44}\text{Ti}$ ,” *The Astrophysical Journal*, vol. 715, no. 2, p. 1383, 2010.
- [4] <http://aspire.cosmic-ray.org/Labs/StarLife/oldstars.html>, “Old stars,” *University of Utah*, accessed 17 April 2020.
- [5] A. Iyudin, *et al.*, “COMPTEL observations of  $^{44}\text{Ti}$  gamma-ray line,” *Astronomy and astrophysics*, vol. 284, 1994.
- [6] J. Vink *et al.*, “Detection of the 67.9 and 78.4 keV lines associated with the radioactive decay of  $^{44}\text{Ti}$  in Cassiopeia A,” *The Astrophysical Journal*, vol. 560, pp. L79–L82, oct 2001.
- [7] M. Renaud *et al.*, “The signature of  $^{44}\text{Ti}$  in Cassiopeia A revealed by IBIS/ISGRI on INTEGRAL,” *The Astrophysical Journal Letters*, vol. 647, no. 1, p. L41, 2006.
- [8] B. Grefenstette *et al.*, “Asymmetries in core-collapse supernovae from maps of radioactive  $^{44}\text{Ti}$  in Cassiopeia A,” *Nature*, vol. 506, no. 7488, pp. 339–342, 2014.
- [9] S. Grebenev, A. Lutovinov, S. Tsygankov, and C. Winkler, “Hard-x-ray emission lines from the decay of  $^{44}\text{Ti}$  in the remnant of supernova 1987A,” *Nature*, vol. 490, no. 7420, pp. 373–375, 2012.
- [10] R. Diehl, N. Prantzos, and P. von Ballmoos, “Astrophysical constraints from gamma-ray spectroscopy,” *Nuclear Physics A*, vol. 777, pp. 70 – 97, 2006. Special Issue on Nuclear Astrophysics.

- [11] P. A. Young *et al.*, “Constraints on the progenitor of Cassiopeia A,” *The Astrophysical Journal*, vol. 640, no. 2, p. 891, 2006.
- [12] L.-S. The, D. D. Clayton, L. Jin, and B. S. Meyer, “Nuclear reactions governing the nucleosynthesis of  $^{44}\text{Ti}$ ,” *The Astrophysical Journal*, vol. 504, pp. 500–515, sep 1998.
- [13] L.-S. The *et al.*, “Are  $^{44}\text{Ti}$ -producing supernovae exceptional?,” *Astronomy and Astrophysics*, vol. 450, p. 1037–1050, Apr 2006.
- [14] S. Nagataki, M. Hashimoto, K. Sato, and S. Yamada, “Explosive nucleosynthesis in axisymmetrically deformed type II supernovae,” *The Astrophysical Journal*, vol. 486, no. 2, p. 1026, 1997.
- [15] G. Magkotsios, F. X. Timmes, A. L. Hungerford, C. L. Fryer, P. A. Young, and M. Wiescher, “Trends in  $^{44}\text{Ti}$  and  $^{56}\text{Ni}$  from core-collapse supernovae,” *The Astrophysical Journal Supplement Series*, vol. 191, no. 1, p. 66, 2010.
- [16] A. Sonzogni *et al.*, “The  $^{44}\text{Ti}(\alpha, p)$  reaction and its implication on the  $^{44}\text{Ti}$  yield in supernovae,” *Physical review letters*, vol. 84, no. 8, p. 1651, 2000.
- [17] V. Margerin *et al.*, “Study of the  $^{44}\text{Ti}(\alpha, p)^{47}\text{V}$  reaction and implications for core collapse supernovae,” *Physics Letters B*, vol. 731, pp. 358 – 361, 2014.
- [18] W. Hauser and H. Feshbach, “The inelastic scattering of neutrons,” *Physical review*, vol. 87, no. 2, p. 366, 1952.
- [19] K. Krane, “Introductory nuclear physics,” pp. 424–431, 1988.
- [20] M. Kawai, A. Kerman, and K. McVoy, “Modification of Hauser-Feshbach calculations by direct-reaction channel coupling,” *Annals of Physics*, vol. 75, no. 1, pp. 156–170, 1973.
- [21] K. A. Chipps, P. Adsley, M. Couder, W. R. Hix, Z. Meisel, and K. Schmidt, “Evaluation of experimental constraints on the  $^{44}\text{Ti}(\alpha, p)^{47}\text{V}$  reaction cross section relevant for supernovae,” *Physical Review C*, vol. 102, no. 3, p. 035806, 2020.
- [22] A. Cowley, “Two-nucleon transfer reactions and implications for studies of exotic nuclei,” in *Exotic Nuclei: Proceedings of the First International African Symposium*, pp. 333–342, World Scientific, 2015.
- [23] A. M. Long, T. Adachi, M. Beard, G. Berg, Z. Buthelezi, J. Carter, M. Couder, R. de-Boer, R. Fearick, S. Förtsch, *et al.*, “Indirect study of the stellar  $^{34}\text{Ar}(\alpha, p)^{37}\text{K}$  reaction rate through  $^{40}\text{Ca}(p, t)^{38}\text{Ca}$  reaction measurements,” *Physical Review C*, vol. 95, no. 5, p. 055803, 2017.

- [24] J. Brummer, *Spectroscopy of  $^{22}\text{Mg}$  relevant to explosive nucleosynthesis in classical novae and X-ray bursts*. PhD thesis, Stellenbosch University, 2020.
- [25] R. Neveling, H. Fujita, F. Smit, T. Adachi, G. Berg, E. Buthelezi, J. Carter, J. Conradie, M. Couder, R. Fearick, *et al.*, “High energy-resolution zero-degree facility for light-ion scattering and reactions at iThemba LABS,” *Nuclear Instruments and Methods in Physics Research Section A: Accelerators, Spectrometers, Detectors and Associated Equipment*, vol. 654, no. 1, pp. 29–39, 2011.
- [26] <https://www.nndc.bnl.gov/qcalc/>, “NNDC, Brookhaven National Laboratory, Q-value calculator (QCalc),” accessed 19 August 2021.
- [27] C. Iliadis, *Nuclear physics of stars*. John Wiley & Sons, 2015.
- [28] N. Bohr, “Neutron capture and nuclear constitution,” *Nature*, vol. 137, no. 3461, pp. 344–348, 1936.
- [29] T. Rauscher, F.-K. Thielemann, and K.-L. Kratz, “Nuclear level density and the determination of thermonuclear rates for astrophysics,” *Physical Review C*, vol. 56, no. 3, p. 1613, 1997.
- [30] V. Zelevinsky and M. Horoi, “Nuclear level density, thermalization, chaos, and collectivity,” *Progress in Particle and Nuclear Physics*, vol. 105, pp. 180–213, 2019.
- [31] A. Koning *et al.*, “Talys-1.95, a nuclear reaction program,” 2019.
- [32] S. Goriely, S. Hilaire, and A. J. Koning, “Improved microscopic nuclear level densities within the Hartree-Fock-Bogoliubov plus combinatorial method,” *Phys. Rev. C*, vol. 78, p. 064307, Dec 2008.
- [33] R. Capote, M. Herman, P. Obložinský, P. Young, S. Goriely, T. Belgya, A. Ignatyuk, A. J. Koning, S. Hilaire, V. A. Plujko, *et al.*, “RIPL—reference input parameter library for calculation of nuclear reactions and nuclear data evaluations,” *Nuclear Data Sheets*, vol. 110, no. 12, pp. 3107–3214, 2009.
- [34] <https://tlabs.ac.za/>, “iThemba LABS,” accessed 18 April 2021.
- [35] M. Jingo, *Fine structure of the Isovector Giant Dipole Resonance: a survey with the  $(p,p')$  reaction at zero degrees*. PhD thesis, University of the Witwatersrand, Johannesburg, 2014.
- [36] P. Adsley, R. Neveling, P. Papka, Z. Dyers, J. Brümmer, C. A. Diget, N. Hubbard, K. Li, A. Long, D. Marin-Lambarri, *et al.*, “CAKE: the coincidence array for k600 experiments,” *Journal of Instrumentation*, vol. 12, no. 02, p. T02004, 2017.

- [37] <http://magnet.web.psi.ch/Analysis/track.html>, “Program track, v8.6, magnet section, Paul Scherrer Institute (PSI), Switzerland,” accessed 18 April 2021.
- [38] *Experiment PR242 Logbook 1*. Unpublished, 2015.
- [39] A. Long, *Indirect study of the stellar  $^{34}\text{Ar}(\alpha, p)^{37}\text{K}$  reaction rate through  $^{40}\text{Ca}(p, t)^{38}\text{Ca}$  reaction measurements*. PhD thesis, University of Notre Dame, 2016.
- [40] R. Neveling *et al.*, *Guide to the K600 magnetic spectrometer*. 2018.
- [41] <https://www.crystals.saint-gobain.com/products/plastic-scintillators>, “Saint-Gobain crystals, plastic scintillators,” accessed 18 April 2021.
- [42] Hamamatsu, “Hamamatsu,” 2022. Available at [https://www.hamamatsu.com/eu/en/product/optical-sensors/pmt/pmt\\_tube-alone/head-on-type/R329-02.html](https://www.hamamatsu.com/eu/en/product/optical-sensors/pmt/pmt_tube-alone/head-on-type/R329-02.html).
- [43] <https://midas.triumf.ca/MidasWiki>, “TRIUMPF MIDAS,” accessed 17 April 2020.
- [44] M. S. Basunia, “Nuclear data sheets for  $A = 22$ ,” *Nuclear Data Sheets*, vol. 127, pp. 69–190, 2015.
- [45] S. Das, “A simple alternative to the crystal ball function,” *arXiv preprint arXiv:1603.08591*, 2016.
- [46] C. Wheldon, “Derivation for two-body kinematics,” 2012. Available at [http://www.np.ph.bham.ac.uk/research\\_resources/programs/ckin/kinematics.pdf](http://www.np.ph.bham.ac.uk/research_resources/programs/ckin/kinematics.pdf).
- [47] J. F. Ziegler, M. D. Ziegler, and J. P. Biersack, “SRIM—the stopping and range of ions in matter (2010),” *Nuclear Instruments and Methods in Physics Research Section B: Beam Interactions with Materials and Atoms*, vol. 268, no. 11-12, pp. 1818–1823, 2010.
- [48] D. Tilley, J. Kelley, J. Godwin, D. Millener, J. Purcell, C. Sheu, and H. Weller, “Energy levels of light nuclei  $A=8,9,10$ ,” *Nuclear Physics A*, vol. 745, no. 3, pp. 155–362, 2004.
- [49] F. Ajzenberg-Selove, “Energy levels of light nuclei  $A = 13-15$ ,” *Nuclear Physics A*, vol. 523, no. 1, pp. 1–196, 1991.
- [50] J. Bruandet, N. Longequeue, J. Longequeue, and B. Vignon, “Spectroscopie du  $^{48}\text{Cr}$  obtenue par réaction  $^{50}\text{Cr}(p, t)^{48}\text{Cr}$ ,” *Physics Letters B*, vol. 37, no. 1, pp. 58–60, 1971.
- [51] W. Dorenbusch, J. Ball, R. Auble, J. Rapaport, and T. Belote, “Energy levels in  $^{48}\text{Cr}$  observed in the  $^{50}\text{Cr}(p, t)^{48}\text{Cr}$  reaction,” *Physics Letters B*, vol. 37, no. 2, pp. 173–176, 1971.
- [52] J. Shepard, R. Graetzer, and J. Kraushaar, “The level structure of  $^{48}\text{Cr}$  and  $^{68}\text{Ge}$  from the  $(p,t)$  reaction at  $E_p = 27$  MeV,” *Nuclear Physics A*, vol. 197, no. 1, pp. 17–32, 1972.

- [53] T. Burrows, “Nuclear data sheets for  $A = 48$ ,” *Nuclear Data Sheets*, vol. 107, no. 7, pp. 1747–1922, 2006.
- [54] W. Alford, R. Lindgren, D. Elmore, and R. Boyd, “ $J\pi = 0^+$  states in the (fp) shell excited in the ( $^3\text{He}, n$ ) reaction,” *Nuclear Physics A*, vol. 243, no. 2, pp. 269–297, 1975.
- [55] D. Evers, W. Assmann, K. Rudolph, S. Skorka, and P. Sperr, “The ( $^3\text{He}, n$ ) reaction on even (f, p) shell nuclei at 15, 18 and 21 MeV (ii),” *Nuclear Physics A*, vol. 230, no. 1, pp. 109–140, 1974.
- [56] J. Szerypo, D. Bazin, B. Brown, D. Guillemaud-Mueller, H. Keller, R. Kirchner, O. Klepper, D. Morrissey, E. Roeckl, D. Schardt, and B. Sherrill, “The beta decay of  $^{48}\text{Mn}$ : Improved data on gamow-teller quenching,” *Nuclear Physics A*, vol. 528, no. 1, pp. 203–214, 1991.
- [57] D. E. Alburger, “Nuclear data sheets for  $a = 48$ ,” *Nucl.Data Sheets*, vol. 45, p. 557, 1985.